

Response to the Comments of Reviewer #1

The manuscript attempts to address the mechanisms of Arctic amplification of climate warming and sea ice loss. Cyclostationary empirical orthogonal functions are applied on ERA-Interim reanalysis products, and the methodology 5 includes novel aspects. Some interesting results are found on the relationships between turbulent surface fluxes, longwave radiation, and sea ice loss. After substantial revisions the manuscript has potential for a good paper in *The Cryosphere*.

Major comments

10 **Comment1(C1):** The authors focus on the statistical relationships of the spatial patterns of anomalies in wintertime sea ice concentration, turbulent surface fluxes of sensible and latent heat, upward and downward longwave radiation, as well as air temperature, humidity and total cloud cover. Both the Arctic amplification and sea ice loss are, however, much more complicated processes, involving many factors, such as the large-scale atmospheric transports of heat and moisture from lower latitudes to the Arctic, and oceanic transports of heat and freshwater. Also, the role of clouds in the Arctic climate 15 system cannot be characterized simply by the total cloud cover; the cloud water and ice contents are at least equally important, as are also the complex interactions between the surface fluxes, boundary-layer turbulence, cloud physics and radiative transfer. I don't mean that the authors should address all these processes, but they should make it clear in the manuscript that they restrict to processes acting in the Arctic, ignoring the forcing from lower latitudes, and they should pay more attention to cloud water and ice contents, which are physically more meaningful variables than the total cloud cover 20 based on reanalysis.

Response1(R1): We thank the reviewer for detailed and constructive comments on the manuscript. As the reviewer mentioned, there are other processes, particularly forcing from lower latitudes, which are important for Arctic amplification and sea ice reduction. As can be seen in Figure R1, there is a net convergence of moisture transport and heat transport over 25 the region of sea ice reduction, although the center of action is over the Greenland Sea. Thus, moisture and heat transport from lower latitudes apparently affects the variation of sea ice concentration. Figure R2 further shows that there is an appreciable correlation between the specific humidity variation and convergence of moisture transport (corr=0.62) and between the lower tropospheric temperature and convergence of heat transport (corr=0.33). Thus, it seems that both the convergence of moisture transport and the convergence of heat transport are at least partly responsible for the variation of 30 specific humidity and temperature in the lower troposphere. On the other hand, the convergence of horizontal transport of moisture cannot explain one essential element of specific humidity anomaly—the mean of anomalous specific humidity. As can be seen in Figure R2a, the mean of moisture convergence is close to 0.6×10^{-6} g/kg/sec, which amounts to ~ 0.05 g/kg of moisture. This value explains only about 17% of the mean value of anomalous specific humidity (~ 0.3 g/kg); the remainder

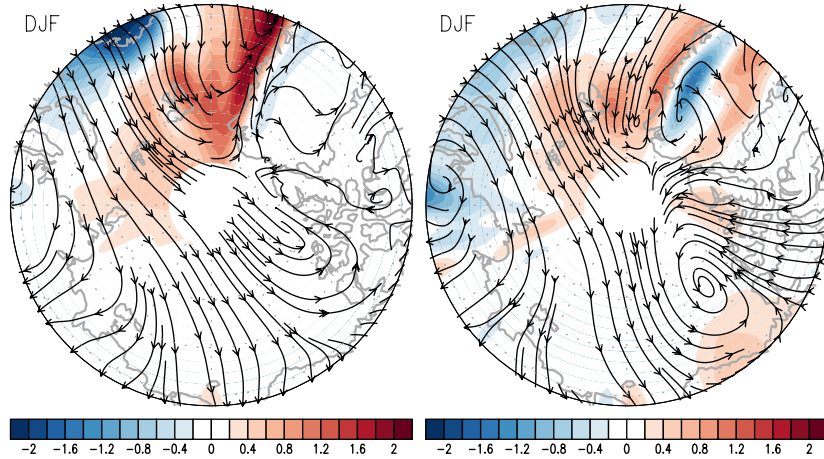


Figure R1. Winter-averaged (left panel) moisture transport (streamline) and its convergence (shade) and (right panel) heat transport (streamline) and its convergence (shade) in the lower troposphere (1000-850 hPa) associated with the sea ice loss mode.

should derive from a vertical process. Consider the following moisture conservation equation:

$$\frac{\partial q}{\partial t} = -\vec{u} \cdot \nabla q + S = -\nabla \cdot (q\vec{u}) + S = -\nabla_h \cdot (q\vec{u}) - \frac{\partial (q_w)}{\partial z} + S.$$

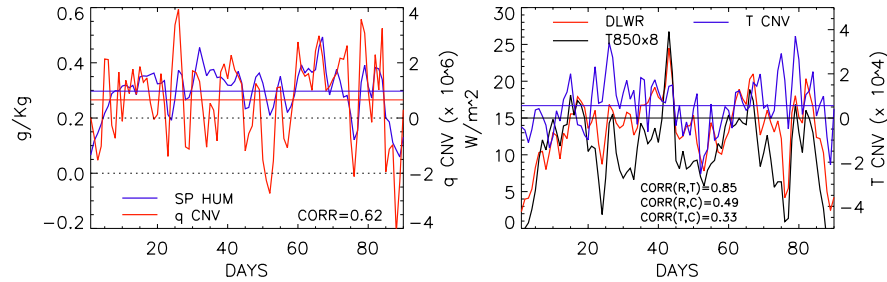


Figure R2. The daily time series of anomalous specific humidity and anomalous moisture convergence averaged over the sea ice loss region (21° - 79.5° E \times 75° - 79.5° N) in the Barents-Kara Seas. These time series are derived from the regressed loading vectors associated with the sea ice loss mode.

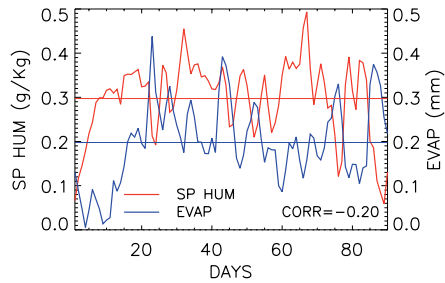


Figure R3. The daily variation of specific humidity (red) and evaporation (blue) averaged over the region of sea ice reduction (21° - 79.5° E \times 75° - 79.5° N) in the Barents-Kara Seas.

5

The convergence of the horizontal moisture transport is not so effective as the convergence of the vertical moisture transport in the equation above. As can be seen in Fig. R3, the anomalous evaporation due to sea ice reduction is positive throughout the winter and its magnitude is reasonable in comparison with the increase in specific humidity. The two time series in Fig. R3 are negatively correlated (except for the mean), indicating that increase (decrease) in specific humidity due to positive 10 (negative) convergence of moisture transport decreases (increases) evaporation from the surface of the ocean; this is a reasonable explanation according to the bulk formula.

Likewise, the variation of the thermal advection and the subsequent convergence of the heat flux are highly correlated with the variation of downward longwave radiation and the lower tropospheric (850 hPa) temperature (see Fig. R2b). On the 15 other hand, the small mean value of the convergence of the horizontal heat flux cannot explain the significant nonzero mean of the anomalous downward longwave radiation or the anomalous lower tropospheric (850 hPa) temperature. Thus, we think that the vertical process should be invoked to account for the significant changes in the means of the variables over the Barents-Kara Seas.

20 This is a serious issue and requires more detailed calculation and convincing demonstration, which we do not wish to pursue in the present study. We, however, acknowledge that we restrict ourselves to processes acting in the Arctic, ignoring the forcing from lower latitudes. [P3 L4-5: **It should be noted that our discussion is restricted to processes in the Arctic; forcing from lower latitudes can also be important in the process of Arctic amplification and sea ice reduction.**]

25 We showed the pattern of total cloud cover, since several authors address that radiative forcing produced by clouds is an important mechanism for Arctic amplification. As the reviewer mentioned, cloud liquid water and cloud ice water may be a better measure of the effect of clouds rather than total cloud cover. Figure R4 indeed shows the patterns of total cloud liquid

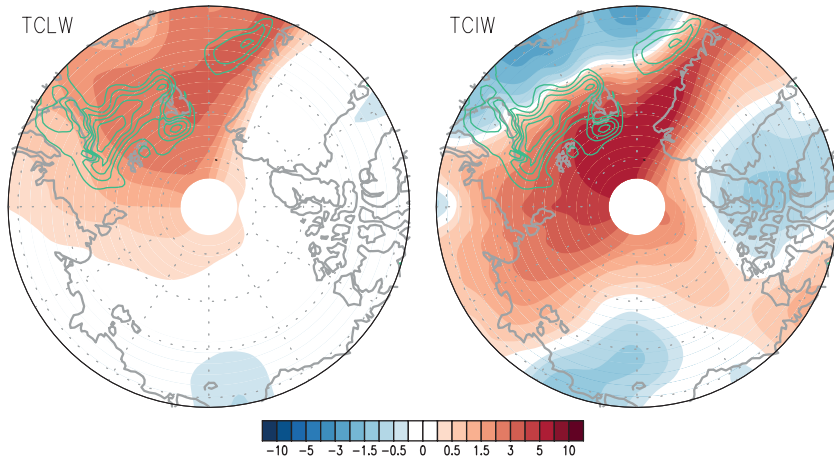


Figure R4. The winter-averaged patterns of total cloud liquid water (left) and total cloud ice water (right) associated with the sea ice loss mode.

5

water and total cloud ice water exhibit better consistency with the region of sea ice reduction. In lieu of this new finding, we will replace the pattern of total cloud cover by the patterns of TCLW and TCIW in Fig. 4. [P5 L17-21: **The patterns of total cloud liquid water and total cloud ice water, which are the key variables for the formation of clouds, also exhibit a strong response over the region of sea ice reduction although their centers of action are shifted toward the Greenland Sea (Fig. 4d).**

10 **The pattern of total cloud cover, however, does not show any strong cloud activity over the region of sea ice reduction (Fig. S3 in the supplementary information); it should be understood that cloud cover is a difficult variable to simulate accurately in a reanalysis model.]**

C2: Atmospheric reanalyses include serious errors in the Polar regions. This is the case particularly for surface fluxes and 15 near-surface meteorological variables (e.g. Jakobson et al., 2012; Tastula et al., 2013). Hence, to obtain more robust results, I suggest to repeat the calculations using a second reanalysis (e.g. NCEP-CFSR) in addition to ERA-Interim.

R2: In response to the reviewer's suggestion, we analyzed a limited number of variables from the NCEP reanalysis product in order to reproduce the key results in the present manuscript. Figure R5 shows the regressed loading vectors derived from 20 the 1979-2016 NCEP reanalysis product with the sea ice loss mode as the target variable. As a comparison between Figs. R5 and R6 shows, there is no essential difference between the two sets of regressed loading vectors except for a small difference

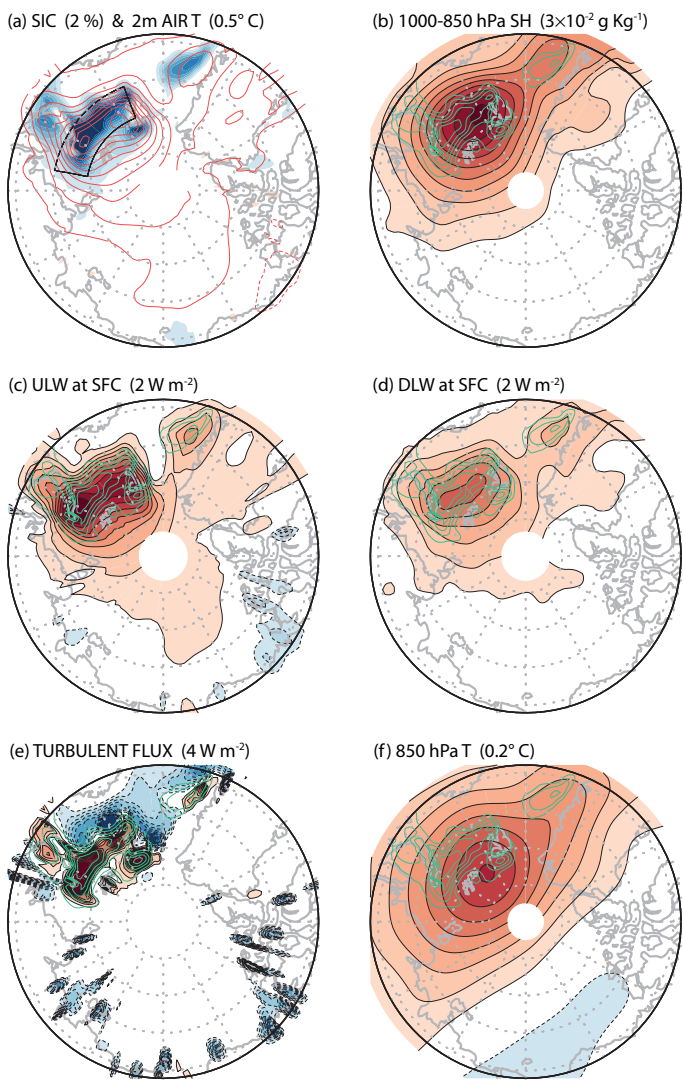


Figure R5. The regressed patterns of atmospheric variables based on the NCEP Reanalysis product (1979-2016). The target is the sea ice loss mode.

(a) SIC (2 %) & 2m AIR T (0.5° C)

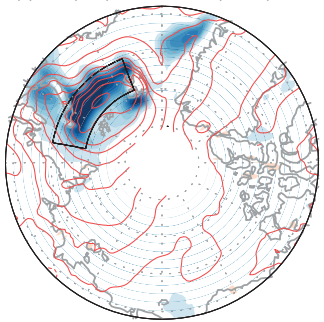
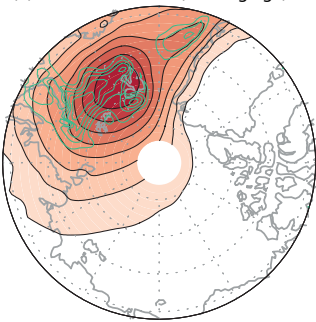
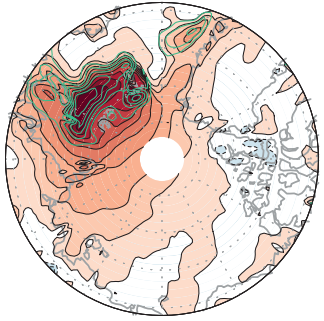
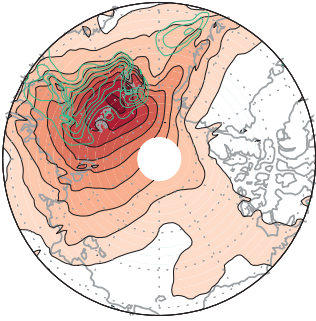
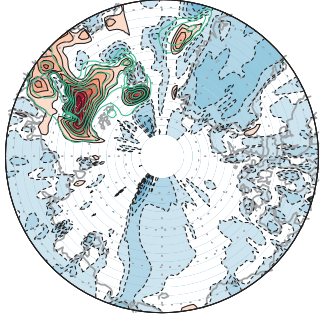
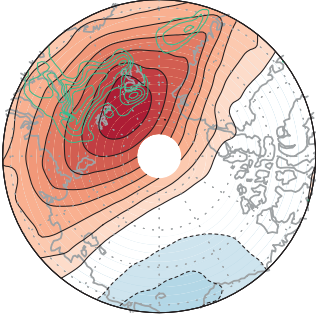
(b) 1000-850 hPa SH ($3 \times 10^{-2} \text{ g Kg}^{-1}$)(c) ULW at SFC (2 W m^{-2})(d) DLW at SFC (2 W m^{-2})(e) TURBULENT FLUX (4 W m^{-2})(f) 850 hPa T (0.2° C)

Figure R6. The regressed patterns of atmospheric variables based on the ERA-Interim reanalysis product (Figure 1a-f in the manuscript).

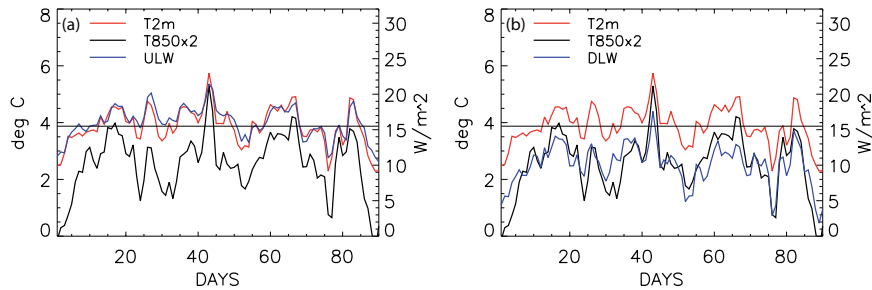


Figure R7. Daily pattern of variability over the region of sea ice loss (21° - 79.5° E \times 75° - 79.5° N) derived from the NCEP reanalysis data: (a) 2 m air temperature (red), 850 hPa air temperature \times 2 (black), and upward longwave radiation (blue), and (b) same as (a) except for the regressed downward longwave radiation (blue). The straight line represents the winter mean value of anomalous 2 m air temperature. Correlation of upward and downward longwave radiation with 2 m air temperature is respectively 0.95 and 0.94, whereas correlation with 850 hPa air temperature is respectively 0.81 and 0.86.

in the scales. This magnitude difference seems to be due to slightly different sensitivity of sea ice to atmospheric and oceanic forcing in the two datasets. This exercise confirms that the behavior of the atmospheric variables in association with the sea ice reduction in the Barents-Kara Seas is not significantly different between the two reanalysis products and the physical mechanism addressed in the present study is not overly sensitive to the choice of a model dataset.

Figure R7 further shows the daily variation of surface (2 m) air temperature, 850 hPa air temperature, upward longwave radiation and downward longwave radiation over the region of sea ice reduction (21° - 79.5° E \times 75° - 79.5° N). As a comparison between Fig. R7 and Fig. 6 in the manuscript shows, the daily variation of derived from the NCEP reanalysis product is fairly similar to that derived from the ERA-Interim product. Again, there is a slight difference in the scales of anomalous variable, but the daily variation derived from the two datasets is not much different (see Figure 6 in the manuscript) confirming that the physical mechanism addressed in the present study is not sensitive to the choice of a dataset.

We added the following statement. [P8 L8-11: Finally, it should be mentioned that the feedback process does not seem to be sensitive to a choice of the dataset. A similar experiment conducted by using the NCEP reanalysis data produces essentially identical results except for a slight overestimation of the strength of the anomalous patterns in Fig. 1a-f and Fig. 6 (see Figs. S5 and S6 in the supplementary information).]

C3: Several results detected from the reanalysis require a better physical explanation.

C3a: Lines 32-33: Why does the region of sea ice loss generate anticyclonic circulation? Figure 3 is not clear in this respect. Show maps of sea level pressure or geopotential height at a relevant pressure level to illustrate this and explain the physical mechanism resulting in an anticyclonic circulation.

R3a: Figures R8a and R8b show the winter-averaged patterns of SAT, and lower-tropospheric circulation associated with the sea ice loss mode. Figures R8c and R8d show the lower tropospheric vertical sections of temperature, geopotential height,

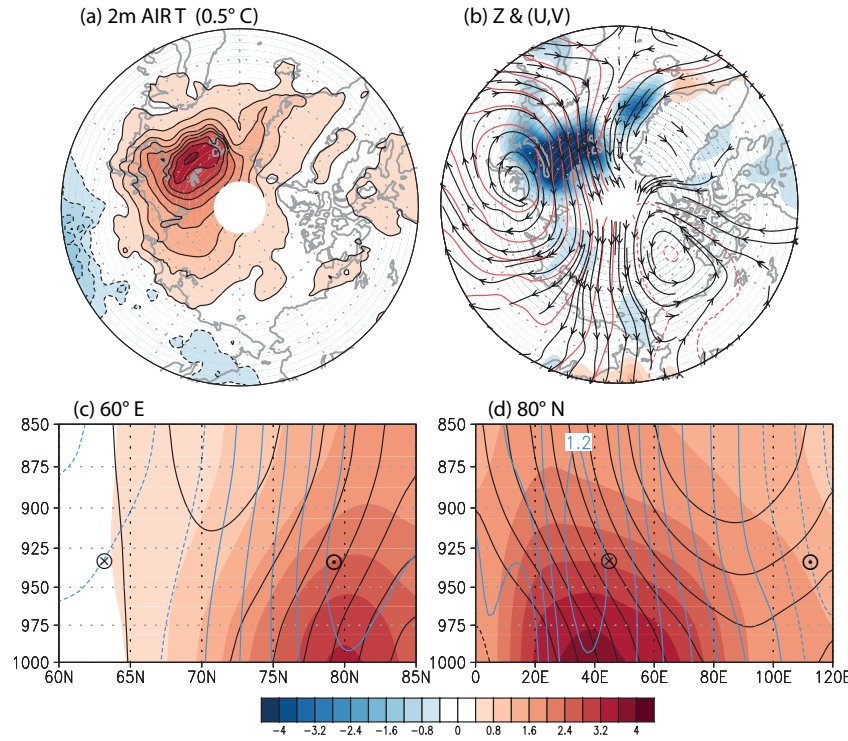


Figure R8. The spatial patterns (60° – 90° N) of (a) 2 m air temperature, and (b) lower tropospheric (1000-900 hPa) geopotential height (red contour) and wind (streamline). (c and d) The lower tropospheric vertical sections of temperature (shade), geopotential height (black contour) and wind (blue contour) along 60° E and 80° N.

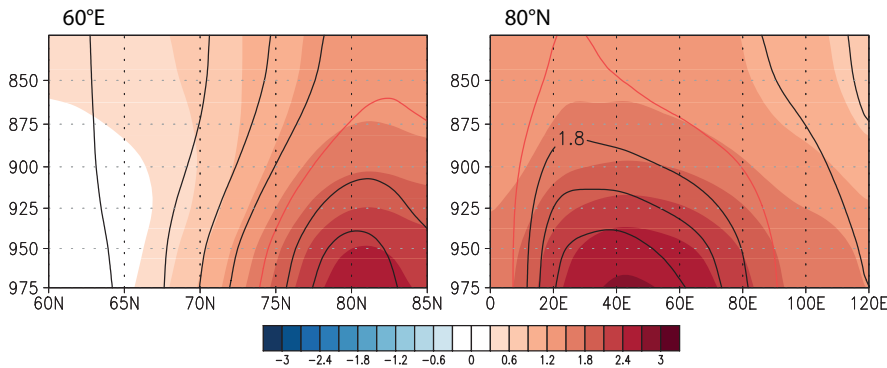


Figure R9. The pressure layer thickness ($\Delta Z = Z(p_1) - Z(p_0)$) derived from the geopotential height pattern in Fig. R8 (shade) and that derived from the hydrostatic equation (contour). The red contour represents the thickness of 1.5 m. The 5 level p_1 is the level used for plotting and p_0 is the pressure level below p_1 at the interval of 25 hPa.

and wind along 60°E and 80°N across the center of action. It is difficult to explain what exactly is happening dynamically based on data analysis alone. Nonetheless, the physical variables in Fig. R8 are physically consistent with each other. For 10 example, the lower tropospheric wind field seems nearly in geostrophic balance with the geopotential height field. Further, Fig. R9 shows that the anomalous geopotential height field is nearly in hydrostatic balance with the anomalous temperature field:

$$(dZ)_j = -\frac{R\langle T \rangle_j}{g} (d \ln p)_j,$$

where

$$(dZ)_j = Z_j - Z_{j-1}, \quad \langle T \rangle_j = (T_j + T_{j-1})/2, \quad (d \ln p)_j = \ln p_j - \ln p_{j-1}.$$

15 Thus, it seems that the release of energy in the form of radiation and heat flux changes the temperature, and geopotential height in the lower troposphere adjusts in accordance with the hydrostatic balance. [new Figure 3: We replaced the 925 hPa air temperature pattern by the lower tropospheric geopotential height and wind pattern.] [P5 L6-8: Figure 3 shows the anomalous surface (2 m) air temperature, the lower tropospheric geopotential height and wind and the vertical section of anomalous temperature, geopotential height and wind along 60°E and 80°N associated with sea ice reduction.] [P5 L10-11: 20 ... consistent according to the hydrostatic equation (see Fig. S2).] [We added relevant discussion in conjunction with Fig. R9 in the supplementary information together with the figure (see Figure S2 and corresponding explanation).]

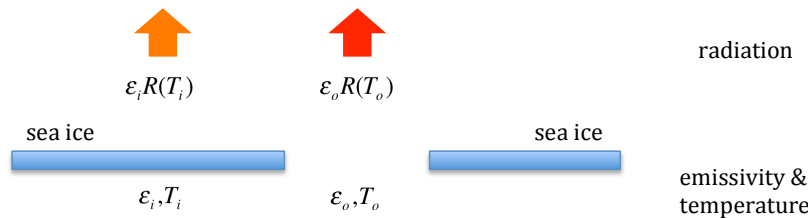
C3b: Page 5, lines 29-30: if the turbulent surface fluxes are upward and net longwave radiation is upwards, they tend to reduce the Earth surface temperature but increase the near-surface air temperature, not decrease it.

R3b: We used the surface (2 m) air temperature as a proxy for the surface temperature, since there is no surface temperature variable in the ERA-Interim reanalysis product. Thus, we assumed that the atmosphere up to 2 m height from the surface essentially behaves the same way as the surface with a negligible absorption of turbulent heat flux. If the anomalous 2 m air temperature is not significantly different than that of surface temperature, the amount of anomalous net longwave radiation at 2 m level would not be much different from that at the surface. Therefore, there would be net deficit of radiation energy at the 2 m level, resulting in a decrease in surface air temperature. As the reviewer indicated, however, surface turbulent fluxes may 10 be consumed to raise the 2 m air temperature although we do not know the amount of energy consumed at this level. Thus, we changed the sentence as follows: [P6 L8-9: **This implies that surface air temperature should decrease, preventing further sea ice reduction.**] See our discussion in Part (c) for more details.

C3c: Page 6, lines 6-7: Why does a change in 2 m air temperature slightly lead the upward longwave radiation? Further, on 15 lines 8-9: an increase in 2-m air temperature does not have a causal effect of increasing the upward longwave radiation (a statistical relationship may naturally exist). The upward longwave radiation at the surface (which is the product archived in ERA-Interim) is controlled by the surface temperature (and emissivity), not by the 2-m air temperature.

R3c: It is difficult to answer why there is a lag between the two variables. In each grid box, upward longwave radiation is 20 computed via (see Fig. R10)

$$ULR(t) = \varepsilon_i(t)R(T_i(t))f_i(t) + \varepsilon_o(t)R(T_o(t))f_o(t), \quad (1)$$



25 Figure R10. A typical situation of calculating upward longwave radiation in each grid box. Upward longwave radiation is calculated for sea ice tile and open ocean tile separately in order to calculate total upward longwave radiation for the grid box. The emissivity and fractional area of sea ice are functions of time.

where $R(t)$ is radiation as a function of radiating temperature T , ε is emissivity, f is a fractional area, the subscripts i and o stand for the “ice-covered” and “open (ice free)” areas, respectively, and $ULR(t)$ denotes the averaged upward longwave radiation in the grid box. In (1), the radiating function (basically Planck function) is a nonlinear function of temperature, and the emissivity ε may be dependent upon the sky condition as well as the surface condition. Further, f varies in time. Thus, 5 the calculation of upward longwave radiation in each grid box may not be a linear function of (grid-averaged) surface temperature. This means that anomalous upward longwave radiation is not a linear function of anomalous surface temperature. Also note that the amount of anomalous radiation is not a function of anomalous temperature; it is determined by the temporally varying background (mean) temperature plus the anomalous temperature. Therefore, the amount of anomalous upward longwave radiation is not simply a function of anomalous surface temperature.

10

The 2 m air temperature change slightly leads the change in upward longwave radiation according to our lagged correlation analysis based on the 3-hourly ERA-Interim data. As can be seen in our original Figure 7 in the manuscript, however, the lead is less than 0.1 days (less than one time step) and the lagged correlation varies little between the lag range of [0, 0.1] day. Thus, we cannot confirm if this lead/lag relationship is a realistic relationship between the two variables or an artifact 15 of analysis. Based on the shape of the lagged correlation (correlation for positive lags is generally stronger than that for negative lags at the same distance from lag 0), we thought that it was reasonable to say that 2m air temperature slightly leads upward longwave radiation.

We used the 2 m air temperature as a proxy for the surface temperature in order to explain changes in upward longwave 20 radiation. As the reviewer mentioned, surface temperature instead of surface air temperature should be used in order to address this issue. Unfortunately, there is no variable called the “surface temperature” in the ERA-Interim product. We could have used the skin temperature T_{SK} but it is defined as the temperature of the surface at radiative equilibrium:

$$R_{SW} + R_{LW} + J_s + L J_q = \Lambda_{skin}(T_{SK} - T_s), \quad (2)$$

where R_{SW} and R_{LW} are shortwave and longwave radiation fluxes at the surface, J_s and J_q are heat and moisture fluxes, Λ_{skin} 25 is skin conductivity, T_s is temperature of soil, snow or ice. It is a poor reflection of radiative energy surplus or deficit at the surface, since any surplus/deficit of radiative energy is compensated by turbulent fluxes and/or heat conduction between the level of skin temperature and the underlying soil, snow or ice. Further, skin temperature is identical with sea surface temperature over ice-free regions. Thus, change in net longwave radiation is not reflected in the skin temperature over the open ocean.

30

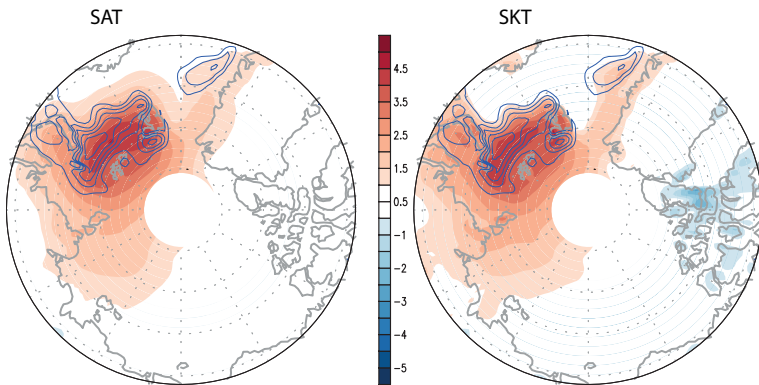
Table R1. Correlation of the loading vectors of 850 hPa air temperature (T_850), upward longwave radiation (ULW), downward longwave radiation (DLW), and net longwave radiation (NLW) with surface air temperature (SAT) in the second column and with skin temperature (SKT) in the third column.

	T_850	ULW	DLW	NLW
SAT	0.861	0.878	0.916	0.681
SKT	0.448	0.891	0.722	0.286

5

The use of skin temperature does not improve the interpretation of the analysis results. As seen in Table R1, skin temperature is slightly better correlated with upward longwave radiation, but exhibits much poorer correlation with downward longwave radiation, net longwave radiation or 850 hPa air temperature for the sea ice loss mode. As seen in Fig. R11, the spatial patterns of the two variables are essentially identical particularly over the region of sea ice reduction in the Barents-Kara Seas. Thus, the use of skin temperature instead of surface air temperature does not alter or improve the physical interpretation of the analysis results in the present study. Neither could we confirm that surface air temperature leads the upward longwave radiation, nor could we find a suitable variable to replace the surface temperature. Therefore, only option we have is to remove the statement about the lead/lag relationship between the surface air temperature and the upward longwave radiation. We modified Figs. 7b and 8, and the corresponding discussion as follows. [P6 L21-22: ...

15 downward longwave radiation, which leads to a sea ice reduction. As a result, surface temperature and upward longwave radiation may increase.] [new Figure 7b & Figure 8]



20 Figure R11. The regressed patterns of surface air temperature (SAT) and skin temperature (SKT) with the sea ice loss mode as the target (contour).

Further, on line 10: Instead of a causal effect from upward longwave radiation to sea ice concentration change, a reduction of sea ice concentration in winter must have an immediate effect in strongly increasing the upward longwave radiation.

We agree with the reviewer. We used the increased upward longwave radiation as an evidence of the increased surface temperature, which eventually leads to sea ice reduction. As the reviewer mentioned, however, sea ice reduction immediately increases the upward longwave radiation because of the exposure of higher sea surface temperature. Thus, the lead/lag relationship between the upward longwave radiation and sea ice reduction is not so straightforward. We removed the following sentence: [P6 L22: ~~Further, both downward and upward longwave radiation changes seem to lead sea ice concentration change.~~] At the same time, we modified Figure 8 to reflect this change. [new Figure 8]

10

C3d: Page 6, line 13: related to the above, I suggest removing the words “surface air temperature increases and”.

R3d: We followed the suggestion of the reviewer. [P6 L25: As a result, ~~surface air temperature increases and~~ sea ice melts]

15

Minor comments

C1: Page 2, line 7: I think Vihma (2014) should be dropped from this line.

5

R1: We removed the Vihma (2014) reference. [P2 L7: Vihma (2014) is removed now.]

C2: Page 2, lines 13-17: During spring and early summer the albedo decreases from roughly 0.85 of dry snow-covered ice to 0.4 of melting ice. Hence, the albedo feedback is important already during the snow and ice melt, already before the 10 appearance of open sea.

R2: We modified the sentence as follows: [P2 L17-18: ... absorbing atmospheric heat during summer. **The albedo feedback is also important during the snow and ice melt in spring and early summer even before the appearance of open sea.**]]

15 C3: Page 2, line 18: the term “oceanic heat transport” is not the best possible, as it may be interpreted as the horizontal transport from lower latitudes to the Arctic.

R3: We modified the sentence as follows: [P2 L19-20: ... **mechanism becomes oceanic horizontal advection and vertical convection of heat** (Screen and Simmonds, 2010b).]

20

C4: Equation 1 and the text below: explain what is r .

R4: We modified the sentence as follow: [P3 L16: ... physical process, $T_n(t)$ describes ... on a longer time scale, **and r and t denote location and time, respectively.**]

25

C5: Page 4, line 23: On the basis of Figure 2, I would not write that the sea ice concentration remains nearly stationary throughout the winter.

R5: We modified the sentence as follows: [P5 L1-2: **Sea ice concentration varies slightly on a daily basis, and its fluctuation is less than 2% from the mean value of -14.7% throughout the winter (Fig. 2).**]

C6: Page 4, line 25: I cannot detect the 40% decrease from the amplitude time series. Also, better explain what the amplitude represents.

R6: As shown in (1), actual data is obtained by multiplying each loading vector with corresponding PC (amplitude) time series. According to Fig. 1g, the amplitude time series has increased by about 2.6 during the 37-year period. Multiplying this value with 14.7% (loading vector; Fig. 2), we obtain ~38.2%. Actually, Fig. 1h is obtained by multiplying the PC time series Fig. 1g with the corresponding loading vector Fig. 2. We modified the sentence as follows: [P5 L3-5: **Multiplying the amplitude (PC) time series (Fig. 1g) with the loading vector (Fig. 2) of the sea ice loss mode as in (1), actual sea ice concentration time series is obtained as in Fig. 1h. According to Fig. 1h, sea ice concentration has decreased by ~40% during the last 37 years.**] [Figure 1 caption: ... The red curve in Fig. 1h is obtained by multiplying the loading vector of sea ice concentration (Fig. 1a) averaged in the boxed area with the amplitude time series (Fig. 1g) according to (1). ...]

10

C7: Page 5, line 9: “the little connectivity” between sea ice reduction and total cloud cover may originate from the fact that sea ice reduction generates two effects that compete against each other: increased latent heat flux tends to increase cloudiness but increasing sensible heat flux tends to reduce it.

15 R7: We thank the reviewer for enlightening us. As mentioned in our response to your major comments, we included the total cloud pattern since several authors mention the possible role of clouds for Arctic amplification. See our response to Major Comment #1 above.

20 C8: Page 6, lines 23-25: These are interesting numbers. Please, confirm if these are winter means in 1979-2016 averaged over sea areas north of 60N. It might be interesting to compare them against results of Lüpkes et al. (2008), which show air temperature responses to 1% reduction in sea ice cover in different conditions.

R8: It is the result based on the average over the region of sea ice reduction (21° - 79.5° E \times 75° - 79.5° N) in the Barents-Kara Seas; it shows the values of anomalous radiation and surface fluxes for an average sea ice reduction of ~15% (see Fig. 2).
25 Lüpkes et al. (2008) conducted experiments in different settings using a 1D atmospheric model coupled with snow/sea ice model. Therefore, a rigorous comparison is impossible. Our numbers are smaller than those in Lüpkes et al. but are of the same order of magnitude. It is difficult to explain the reasons for this difference, but the absence of horizontal advection is a plausible cause. In the presence of horizontal advection, anomalous temperature and fluxes over sea ice leads are quickly diffused, resulting in reduced local maxima. We can see a hint of horizontal advection in Fig. 1 in the manuscript; while
30 turbulent heat flux is nearly confined to the area of sea ice loss, 2 m air temperature and other variables are smoothed out over a much wider area. We would rather not include this discussion in the revised text, since we eliminated 2 m air temperature increase in the feedback loop. Moreover, our explanation above is somewhat premature and conjectural in nature. [no modification]

C9: Figure 2. Is plot (a) needed at all, as the same line appears in plot (b)?

R9: We removed Figure 2a. [new Figure 2]

5 C10: Figure 4. Add information on colour scales and absolute values. Only the contour intervals are given.

R10: We revised Figure 4 in order to provide the necessary information the reviewer asked. [new Figure 4; figure caption: The red contour is drawn at the value of the contour interval.]

10 C11: Figure 5. Does the shading represent sea ice concentration in all four plots? If yes, why it includes small differences between the plots?

R11: We accidentally used different shading interval for the sea ice concentration field in Fig. 5c. We corrected the figure. [new Figure 5]

15

C12: Figure 6. Explain better how the time series in days should be interpreted. It cannot be the mean over 1979-2016. Is it from some selected year?

R12: It is the plot of regressed loading vector $B_1(r, t)$ of the sea ice loss mode averaged over the region of sea ice loss (21° -
20 $79.5^\circ\text{E} \times 75^\circ\text{-}79.5^\circ\text{N}$) for different variables. The daily time series are interpreted as typical winter variation of surface fluxes and radiation associated with the sea ice reduction in Fig. 2. Actual data associated with the sea ice loss mode is obtained by multiplying the loading vector with the corresponding PC time series, i.e., the space-time evolution pattern associated with the sea ice loss mode is $T^{(1)}(r, t) = B_1(r, t)T_1(t)$. Thus, the typical time series of surface fluxes and radiation depicted in Fig. 6 are amplifying according to Fig. 1g. We added more description on this figure. [P5 L28-30:
25 Figure 6 shows the winter daily variations of the regressed loading vectors in (6) (terms in curly braces) averaged over the region of sea ice reduction ($21^\circ\text{-}79.5^\circ\text{ E} \times 75^\circ\text{-}79.5^\circ\text{ N}$); it may be interpreted as the atmospheric response to the sea ice reduction shown in Fig. 2.]

C13: Figure 8. Referring to my previous comments, I suggest dropping “2m T increase (0.24)” from the figure, and drawing
30 an arrow directly from increased LW-down to sea ice reduction. Otherwise, provide a good explanation on the causality of the link.

R13: We followed the suggestion of the reviewer. [new Figure 8]

References:

Jakobson, E., T. Vihma, T. Palo, L. Jakobson, H. Keernik, and J. Jaagus (2012). Validation of atmospheric reanalyses over the central Arctic Ocean, *Geophys. Res. Lett.* 39, L10802, doi:10.1029/2012GL051591.

5 Tastula, E.-M., T. Vihma, E. L. Andreas, and B. Galperin (2013), Validation of the diurnal cycles in atmospheric reanalyses over Antarctic sea ice, *J. Geophys. Res. Atmos.*, 118, 4194–4204, doi:10.1002/jgrd.50336.

Understanding the Mechanism of Arctic Amplification and Sea Ice Loss

Kwang-Yul Kim¹, Jinju Kim¹, Saerim Yeo², Hanna Na³, Benjamin D. Hamlington⁴, and Robert R. Leben⁵

¹School of Earth and Environmental Sciences, Seoul National University, 1 Gwanak-ro, Gwanak-gu, Seoul 08826, Republic of Korea

²APEC Climate Center 1463, Haeundae-gu, Busan 48058, Republic of Korea

³Ocean Circulation and Climate Research Center, Korea Institute of Ocean Science and Technology, Ansan, 15627, Republic of Korea

⁴Department of Ocean, Earth and Atmospheric Sciences, 4600 Elkhorn Avenue, Room 406, Old Dominion University, Norfolk, Virginia 23529, USA

⁵Colorado Center for Astrodynamics Research, Department of Aerospace Engineering Sciences, ECNT 320, 431 UCB, University of Colorado, Boulder, Colorado 80309-0431, USA

15 Correspondence to: Kwang-Yul Kim (kwang56@snu.ac.kr)

Abstract. Sea ice reduction is accelerating in the Barents and Kara Seas. Several mechanisms are proposed to explain the accelerated loss of polar sea ice, which remains an open question. In the present study, the detailed physical mechanism of sea ice reduction in winter is identified using the daily ERA interim reanalysis data. Downward longwave radiation is an essential element for sea ice reduction, but can only be sustained by excessive upward heat flux from the sea surface exposed to air in the region of sea ice loss. The increased turbulent heat flux is used to increase air temperature and specific humidity in the lower troposphere, which in turn increases downward longwave radiation. This feedback process is clearly observed in the Barents and Kara Seas in the reanalysis data. A quantitative assessment reveals that this feedback process is amplifying at the rate of ~8.9 % every year during 1979-2016. Based on this estimate, sea ice will completely disappear in the Barents and Kara Seas by as early as 2025, although a conservative linear fit delays it until 2065. Availability of excessive heat flux is necessary for the maintenance of this feedback process; a similar mechanism of sea ice loss is expected to take place over the sea-ice covered polar region when sea ice is not fully recovered in winter.

Jinju Kim 7/7/2017 10:18 AM

Deleted: around 2025

Jinju Kim 7/7/2017 9:48 AM

Deleted: .

1 Introduction

Over the past decades, rapidly enhanced atmospheric warming has been observed in the Arctic (Serreze and Francis, 2006; Bekryaev et al., 2010; IPCC, 2013). The accelerated warming is pronounced in the lower troposphere during the cold season (Serreze et al., 2009; Screen and Simmonds, 2010a; Screen et al., 2013). An accompanying drastic reduction of sea ice (Comiso et al., 2008; Comiso, 2012) has profound implications for global climate changes by affecting energy exchange between ocean and atmosphere (Serreze and Barry, 2011), and is often referred to as a key factor for accelerated warming in the Arctic (Holland and Bitz, 2003; Serreze et al., 2007; Screen and Simmonds, 2010a; Kumar et al., 2010). A particularly

significant sea ice reduction can be found over the Barents and Kara seas, which potentially influences cold winter extremes over the Eurasian continent (Petoukhov and Semenov, 2010; Overland et al., 2011; Tang et al., 2013; Cohen et al., 2014; Mori et al., 2014; Kim et al., 2014; Kim and Son, 2016). Physically, sea ice loss involves a positive ice-atmosphere feedback, which leads to an enhanced warming signal in the Arctic region. This feature is generally referred to as Arctic amplification (Screen and Simmonds, 2010a; Serreze and Barry, 2011) and is expected to persist for at least the next decade (IPCC, 2013; Koenigk et al., 2013).

Jinju Kim 7/7/2017 9:54 AM

Deleted: ; Vihma 2014

Previous studies have proposed the physical mechanisms of Arctic amplification, which involve the effect of atmospheric heat transport (Graversen et al., 2008), oceanic heat transport (Årthun et al., 2012; Chylek et al., 2009; Spielhagen et al., 2011; Onarheim et al., 2015), cloud and water vapor changes (Francis and Hunter, 2007; Schweiger et al., 2008; Park et al., 2015a; Park et al., 2015b), and/or diminishing sea ice cover (Serreze et al., 2009; Screen and Simonds, 2010a; Kim et al., 2016). The accurate physical process of the Arctic amplification, however, is subject to debate.

Due to the large seasonal variation of insolation, there exists pronounced seasonality in the air-sea interaction process over the Arctic Ocean. During summer, open water readily absorbs solar radiation, which results in increasing heat content in the oceanic mixed layer. This represents the so-called albedo feedback (Deser et al., 2000; Serreze et al., 2009; Screen and Simmonds., 2010a; Deser et al., 2010; Serreze and Barry, 2011), meaning that the Arctic Ocean is efficient in absorbing atmospheric heat during summer. The albedo feedback is also important during the snow and ice melt in spring and early summer even before the appearance of open sea. After sunsets over the Arctic Ocean, the ice-albedo feedback is suppressed and the primary air-sea interaction mechanism becomes oceanic horizontal advection and vertical convection heat (Screen and Simmonds, 2010b). The stored heat in the ocean mixed layer is released back to the colder atmosphere above, which will result in warming of the atmosphere. The decreased insulation effect (Screen and Simmonds, 2010b) due to the loss of sea ice also promotes further sea ice reduction. Thus, heat transfer between the ocean and atmosphere is generally considered as the fundamental mechanism of Arctic amplification, which is pronounced only during the cold season. On the other hand, increased cloud cover and water vapor (Francis and Hunter, 2007; Schweiger et al., 2008; Graversen and Wang, 2009; Park et al., 2015a; Park et al., 2015b) can also contribute to an increase in downward longwave radiation.

Jinju Kim 7/7/2017 9:49 AM

Deleted: heat transport

Despite the general consensus that heat transfer between the ocean and atmosphere is a crucial element in the physical mechanism of Arctic amplification and sea ice reduction, a quantitative understanding of individual contributions of heat flux components is still controversial. Further, the role of upward and downward longwave radiations in Arctic amplification is vague and not fully understood. Accurately quantifying the contribution of these different mechanisms, therefore, is required for a complete understanding of the Arctic amplification.

In the present study, a quantitative assessment of energy fluxes involved in the Arctic amplification is investigated in relation to the sea ice reduction over the Barents and Kara Seas. This is an extension of the study by Kim et al. (2016) with a specific goal of delineating the feedback mechanism between sea surface and the atmosphere. In particular, we extract a physically meaningful warming/sea ice reduction signal in the Arctic region and investigate how sea ice loss and individual

energy fluxes are linked in a quantitative manner. For this goal, cyclostationary empirical orthogonal function (CSEOF) analysis is carried out on surface and pressure-level variables derived from the ERA interim daily reanalysis data in winter (Dec. 1-Feb. 28, $d = 90$ days). It should be noted that our discussion is restricted to process in the Arctic; forcing from lower latitudes can also be important in the process of Arctic amplification and sea ice reduction.

5 2 Data and Method of Analysis

2.1 Data

ECMWF Reanalysis (ERA) interim daily variables are used from 1979-2016 (Dee et al., 2011). Both surface and pressure-level variables during winter (Dec. 1-Feb. 28) are analyzed over the Arctic region (north of 60° N) to understand the detailed physical mechanism of sea ice melting and Arctic amplification.

10 2.2 CSEOF analysis and regression analysis in CSEOF space

Analysis tool used for this study is the CSEOF technique (Kim et al., 1996; Kim and North, 1997; Kim et al., 2015). In CSEOF analysis individual physical processes in space-time data are decomposed as:

$$T(r, t) = \sum_n B_n(r, t) T_n(t), \quad B_n(r, t) = B_n(r, t + d), \quad (1)$$

where $B_n(r, t)$ depicts daily winter evolution of the n th physical process and $T_n(t)$ describes how the amplitude of the evolution varies on a longer time scale, and r and t denote location and time, respectively. Since the nested period $d = 90$ days, each loading vector, $B_n(r, t)$, consists of 90 spatial patterns which depict evolution of a variable throughout the winter. These winter evolution patterns, $B_n(r, t)$, repeat every winter, but its amplitude varies from one year to another according to the corresponding PC time series. CSEOF loading vectors are mutually orthogonal to each other in space and time and represent distinct physical processes. The principal component (PC) time series, $T_n(t)$ are uncorrelated with (and are often nearly independent of) each other. Each loading vector depicts a temporal evolution of spatial patterns seen in a physical process (such as El Niño or seasonal cycle), and corresponding PC time series describes a long-term modulation of the amplitude of the physical process. Thus, the CSEOF technique is suitable for extracting and depicting temporal evolution of (nearly independent) physical processes and often yields valuable insight that cannot be attained from single spatial pattern.

In order to make suitable physical interpretation of the analysis results, CSEOF analysis is conducted on a number 25 of key variables. It is, then, extremely important to make CSEOF loading vectors derived from individual variables to be physically consistent with each other. For the purpose of generating physically consistent CSEOF loading vectors, regression analysis is carried out in CSEOF space (Kim et al., 2015). A target variable is chosen such that its major CSEOF modes best depict the physical process under investigation; target variable is sea ice concentration in the present study.

Once CSEOF analysis on the “target” variable is completed as in (1), physically consistent loading vectors of 30 another variable, called the “predictor” variable, are obtained as follows:

Jinju Kim 7/7/2017 9:50 AM
Deleted: are deemed to represent distinct physical processes

Step 1: $P(r, t) = \sum_n C_n(r, t)P_n(t)$ (CSEOF analysis on a new variable) (2)

Step 2: $T_n(t) = \sum_{m=1}^M \alpha_m^{(n)}P_m(t)$ (regression on PC time series) (3)

Step 3: $Z_n(r, t) = \sum_{m=1}^M \alpha_m^{(n)}C_m(r, t)$ (regressed loading vector) (4)

Then, the target and predictor variables can be written as

5 $\{T(r, t), P(r, t)\} = \sum_n \{B_n(r, t), Z_n(r, t)\}T_n(t)$. (5)

Namely, the loading vectors of the two variables, $B_n(r, t)$ and $Z_n(r, t)$, share an identical PC time series, $T_n(t)$, for each mode. As a result, the evolution of a physical process manifested as $B_n(r, t)$ and $Z_n(r, t)$ in two different variables is governed by a single amplitude time series. Otherwise, $B_n(r, t)$ and $Z_n(r, t)$ do not represent the same physical process and henceforth are not physically consistent. This process can be repeated for other predictor variables. As a result of regression,

10 then, entire data can be written in the form

$Data(r, t) = \sum_n \{B_n(r, t), Z_n(r, t), U_n(r, t), \dots\}T_n(t)$, (6)

where the terms in curly braces denote physically consistent evolutions derived from various physical variables. [A rigorous mathematical explanation of the regression analysis in CSEOF space can be found in Kim et al. \(2015\).](#)

15 Aside from the winter seasonal cycle, the first CSEOF mode derived from the daily winter sea ice concentration data in the Arctic depicts sea ice loss and associated Arctic warming in the Barents and Kara Seas. [This mode explains 24% of the total variability of the sea ice concentration in the Arctic Ocean and is the focus of investigation in the present study.](#)

Jinju Kim 7/7/2017 9:52 AM

Formatted: Indent: First line: 1.27 cm

3 Results and Discussion

Figure 1 shows the winter-averaged pattern of $B_1(r, t)$ together with the regressed patterns from other variables (the terms in the curly braces in (6)). We refer to it as the sea ice loss mode, since the loading vector (Fig. 1a; see also Fig. 2) and the 20 amplitude time series (Fig. 1g) describes the sea ice reduction, together with natural variability of sea ice concentration, in the Barents and Kara Seas during the past 37 years (Fig. 1h). [The pattern of sea ice reduction \(Fig. 1a\) is nearly identical with the trend pattern of sea ice concentration in the Arctic Ocean \(see Fig. S1 in the supplementary information\). As can be seen in Fig. 1h, the sea ice reduction trend in the Barents and Kara Seas \(boxed area in Fig. 1a\) is faithfully captured by this mode.](#) In particular, the rate of sea ice loss has significantly increased since 2004-2005 (Vihma, 2014). In association with 25 the sea ice reduction, 2 m air temperature, 850 hPa temperature, specific humidity, upward longwave radiation, downward longwave radiation, and upward heat flux have increased significantly over the region of major sea ice reduction (21° - 79.5° E \times 75° - 79.5° N) (black boxed area in Fig. 1a). As can be seen in Figs. 1a, 1c and 1e, the central areas of anomalous 2 m air temperature, upward longwave radiation and turbulent (sensible + latent) heat flux match well with the region of sea ice loss (Screen and Simmonds, 2010b). On the other hand, the centers of downward longwave radiation and specific humidity 30 match well with that of the 850 hPa air temperature (Figs. 1b, 1d, and 1f).

[Sea ice concentration varies slightly on a daily basis, and its fluctuation is less than 2% from the mean value of -14.7% throughout the winter \(Fig. 2\). In accordance with the reduced sea ice concentration, upward longwave radiation](#)

Jinju Kim 7/7/2017 9:57 AM

Deleted: Sea ice concentration varies slightly on a daily basis, and it remains to be nearly stationary throughout the winter (Fig. 2).

flux is increased from the warmer sea surface exposed to air. Multiplying the amplitude (PC) time series (Fig. 1g) with the loading vector (Fig. 2) of the sea ice loss mode as in (1), actual sea ice concentration time series is obtained as in Fig. 1h. According to Fig. 1h, sea ice concentration has decreased by ~40% during the last 37 years.

Figure 3 shows the anomalous surface (2 m) air temperature the lower tropospheric geopotential height and wind and the vertical section of anomalous temperature, geopotential height and wind along 60°E and 80°N associated with sea ice reduction. A significant warming is seen in the lower troposphere (e.g., Serreze and Francis, 2006; Serreze et al., 2007; Screen et al., 2013). Note that the anomalous temperature pattern is similar to the second EOF pattern in Graversen et al. (2008). The anomalous temperature and geopotential height are consistent according to the hydrostatic equation (see Fig. S2). Anomalous wind and geopotential height are consistent according to the thermal wind equation. As can be seen, an anticyclonic circulation is established over the region of sea ice loss. This anticyclonic circulation results in advection of warmer air over the Barents and Kara Seas and advection of colder air over the mid-latitude East Asia (Kim and Son, 2016).

The winter-averaged patterns of anomalous downward longwave radiation and specific humidity look fairly similar to that of 850 hPa air temperature (Figs. 4a and 4b). It appears that the increased downward longwave radiation is the result of the tropospheric warming (Fig. 3). Specific humidity also increases with the tropospheric warming. Note specifically that these changes are observed over or close to the region of sea ice reduction. The patterns of total cloud liquid water and total cloud ice water, which are the key variables for the formation of clouds, also exhibit a strong response over the region of sea ice reduction although their centers of action are shifted toward the Greenland Sea (Fig. 4d). The pattern of total cloud cover, however, does not show any strong cloud activity over the region of sea ice reduction (Fig. S3 in the supplementary information); it should be understood that cloud cover is a difficult variable to simulate accurately in a reanalysis model. Therefore, we postulate that the increased downward longwave radiation is due to the increased 850 hPa air temperature and the greenhouse effect produced by the increased specific humidity. Further note that net (upward minus downward) longwave radiation is positive over the region of major sea ice reduction, whereas it is slightly negative over the surrounding areas (Fig. 4c). Thus, at the surface level, there is a net loss of longwave energy over the region of sea ice reduction, while there is a net gain of longwave radiation over the surrounding area.

A prominent source of energy available for heating the atmospheric column is the increased turbulent heat flux from the sea surface exposed to air due to sea ice reduction (Fig. 5). Figure 6 shows the winter daily variations of the regressed loading vectors in (6) (terms in curly braces) averaged over the region of sea ice reduction (21°-79.5° E × 75°-79.5° N); it may be interpreted as atmospheric response to the sea ice reduction shown in Fig. 2. Although the total (area-weighted) magnitudes of sensible and latent heat fluxes are generally smaller than those of upward and downward longwave radiation (see Fig. 6a), turbulent heat flux (see Fig. 5) is locally more pronounced than longwave radiations (Deser et al., 2010). Furthermore, the combined effect of turbulent heat flux is about 6 times larger than that of longwave radiation, since upward and downward longwave radiation tends to offset each other and the resulting net longwave radiation is comparatively smaller than the net upward turbulent heat flux (Fig. 6a). In the presence of turbulent heat flux, air temperature and, henceforth, downward longwave radiation can increase continually leading to further sea ice reduction.

Jinju Kim 7/7/2017 9:54 AM

Deleted: Judging from the amplitude time series of the sea ice loss mode (Fig. 1h), sea ice concentration has been reduced by ~40% during the last 35 years.

Jinju Kim 7/7/2017 10:21 AM

Deleted: and

Jinju Kim 7/7/2017 9:55 AM

Deleted: 925 hPa air temperature (upper panels)

Jinju Kim 7/7/2017 9:56 AM

Deleted: The pattern of total cloud cover, on the other hand, differs significantly from that of sea ice concentration or downward longwave radiation (Fig. 4d) (Screen and Simmonds, 2010a). The pattern of total cloud cover associated with the sea ice loss mode does not exhibit any strong cloud activity over the region of sea ice reduction, suggesting little connectivity between sea ice reduction and change in cloud cover. It should be understood, however, that cloud cover is a difficult variable to simulate accurately in a reanalysis model.

While the increased downward longwave radiation is a key element of sea ice reduction, it is not a sustainable physical process by itself. The area-averaged magnitudes of the upward and downward longwave radiation exceed those of the sensible and latent heat flux in the Barents and Kara Seas (Fig. 6a). The net amount of upward longwave radiation, however, is much smaller than the net upward heat flux as a result of near cancellation between the upward and downward longwave radiations. In fact, the upward radiation is, in general, slightly larger than the downward radiation resulting in the net upward longwave radiation of $\sim 2 \text{ W m}^{-2}$ in winter in the Barents and Kara Seas. This implies that surface temperature should decrease, preventing further sea ice reduction. A decrease in surface air temperature also means that tropospheric air temperature should decrease. In this sense, downward longwave radiation alone is not sufficient to sustain the sea ice reduction process. On the other hand, the net amount of heat flux is $\sim 12 \text{ W m}^{-2}$ in the same area. Once ocean surface is exposed due to the reduction of sea ice by ocean current (Schlichtholz, 2011; Smedsrød et al., 2013) or wind (Park et al., 2015b), the enhanced turbulent heat flux helps sustain sea ice reduction.

Jinju Kim 7/7/2017 9:58 AM

Deleted: air

As can be seen in Figs. 6b and 6c, daily upward longwave radiation change over the sea ice loss region is highly correlated with the daily fluctuation of 2 m air temperature, whereas daily downward longwave radiation change is strongly correlated with both 850 hPa and 2 m air temperatures. According to the lagged correlations (Fig. 7), daily changes of both upward and downward longwave radiations in the sea ice loss mode are highly correlated with those of 2 m air temperature and 850 hPa air temperature to a lesser extent. According to analysis based on 3-hourly data, 850 hPa air temperature leads changes in downward longwave radiation. Change in 2 m air temperature, on the other hand, is nearly simultaneous with the downward longwave radiation, whereas it slightly leads the upward longwave radiation. It appears that the increased tropospheric temperature increases the downward longwave radiation, which leads to a sea ice reduction. As a result, surface temperature and upward longwave radiation may increase.

Jinju Kim 7/7/2017 9:58 AM

Deleted: As a result, 2 m air temperature increases and subsequently upward longwave radiation increases. Further, both downward and upward longwave radiation changes seem to lead sea ice concentration change.

Therefore, we propose a feedback mechanism as suggested in Fig. 8. Sea ice reduction in this area leads to an increase in upward heat flux, which is used to raise temperature in the lower troposphere. Warming in the lower troposphere increases downward longwave radiation. As a result, sea ice melts. This feedback process can be written mathematically as follow:

$$25 \quad \text{Step 1: } \frac{dFL^\uparrow}{dt} = -\alpha \frac{dS}{dt}, \quad FL^\uparrow = SW^\uparrow - SW^\downarrow + LW^\uparrow - LW^\downarrow + SF^\uparrow + LF^\uparrow, \quad (7)$$

$$\text{Step 2: } \frac{dT}{dt} = \beta \frac{dFL^\uparrow}{dt}, \quad (8)$$

$$\text{Step 3: } \frac{dLW^\downarrow}{dt} = \gamma \frac{dT}{dt}, \quad (9)$$

$$\text{Step 4: } \frac{dS}{dt} = -\delta \frac{dLW^\downarrow}{dt}, \quad (10)$$

where S is sea ice concentration, T is tropospheric (850 hPa) temperature, LW^\downarrow is downward longwave radiation, and the net upward flux FL^\uparrow is the sum of net short and longwave radiations and sensible and latent heat fluxes. According to the winter

(90-day) averaged loading vector of the sea ice loss mode, $\alpha = 1.016 \times 10^2$, $\beta = 9.522 \times 10^{-2}$, $\gamma = 1.155 \times 10^1$, and $\delta = 8.946 \times 10^{-3}$. It is emphasized that sea ice reduction continues, since downward longwave radiation continues to increase via enhanced upward heat flux from the exposed sea surface. According to our model, 1 % reduction in sea ice coverage leads to 1.02 W m^{-2} increase in upward energy flux, which, in turn, leads to 0.09 K increase in 850 hPa air temperature and 0.91 W m^{-2} increase in downward longwave radiation. ▼

Note that this feedback mechanism, in its present form, does not require any delayed action of increased absorption of insolation during summer in terms of albedo feedback. In winter, a significant amount of turbulent heat flux can be released from the ocean exposed to cold air without excessive energy stored in summer. Summer heating, on the other hand, may be a fortifying factor for this feedback loop by preventing sea ice from refreezing during fall and winter.

10 According to the amplitude time series in Fig. 1g, the rate of sea ice melting appears to be accelerating. A curve fit with an exponential function results in

$$pc(t) = a \exp(\lambda t) + b = a(e^\lambda)^t + b \doteq a(1 + \lambda)^t + b, \quad (11)$$

where $pc(t)$ is the amplitude time series in Fig. 1g, and t is time in years since 1979. We obtained the fitting curve (dashed curve in Fig. 1g) with parameters $a = 1.275 \times 10^{-1}$, $\lambda = 8.916 \times 10^{-2}$, and $b = -9.055 \times 10^{-1}$. Equation (11) can be 15 rewritten as

$$pc(t) - c = (pc(0) - c)(1 + \lambda)^t. \quad (12)$$

That is, the amplitude of sea ice melting and atmospheric warming increases at the rate of $\sim 8.9 \%$ every year.

4 Concluding Remarks

A quantitative estimation of changes in the sea ice and other key variables in the Barents and Kara Seas reveals that increase 20 in downward longwave radiation is sustained by an increase in turbulent flux from the exposed sea surface. While a wider area of sea surface is exposed to air and upward longwave radiation increases due to summer sea surface warming, the increased upward longwave radiation alone seems insufficient to produce a feedback loop. Due to a net deficit of surface radiation in fall/winter, sea ice may refreeze quickly (see Figs. 7 and 8 in Kim et al., 2016). Prolonged sea ice melting is 25 instrumental for increased turbulent flux, which in turn warms the atmospheric column (see Fig. 5). As a result, downward longwave radiation increases and sea ice reduction continues in accordance with surface warming (Fig. 8). This is why significant Arctic amplification is observed only in the Barents and Kara Seas but not in the Laptev, East Siberian or Chukchi Seas, where summer sea ice melting is conspicuous but sea ice quickly refreezes in late fall/early winter (Kim et al., 2016). How sea ice refreezing is delayed in the Barents and Kara Seas remains to be answered. Sea ice cover in the Barents and Kara Seas was $\sim 80 \%$ in 1979 and is currently $\sim 40 \%$. We fitted an exponential curve to the amplitude time series of the sea ice loss mode (Fig. 1g); an exponential fitting is chosen, since it minimizes the residual error. Our calculation shows that sea ice in the sea-ice loss region (21° – 79.5°E , 75° – 79.5°N) of the Barents and Kara Seas may completely melt by as early as 2025 (Fig. 1h) unless impeded by other naturally occurring variability. A quadratic fit results in a similar result (2030 instead

Jinju Kim 7/7/2017 9:59 AM

Deleted: As a result, 2 m air temperature increases by 0.24 K (see Fig. 6).

of 2025). A linear fit, the most conservative of the three but with the largest residual error, predicts a complete disappearance of sea ice in this area by 2065 (see Fig. S4).

It should be pointed out that this feedback process could develop in other areas of the Arctic Ocean. If sea ice refreezing is delayed in late fall/winter, increased turbulent heat flux from the open sea surface will make it more difficult for sea surface to refreeze, ultimately leading to the feedback process in Fig. 8. It is, of course, difficult to determine when this should occur, since environmental factors differ from one location to another. Finally, it should be mentioned that the feedback process does not seem to be sensitive to a choice of the dataset. A similar experiment conducted by using the NCEP reanalysis data produces essentially identical results except for a slight overestimation of the strength of the anomalous patterns in Fig. 1a-f and Fig. 6 (see Figs. S5 and S6 in the supplementary information).

10 5 Data and code availability

All the results of analysis and the programs used in the present paper are freely available by contacting the corresponding author.

15 *Acknowledgments.* This research was supported by the National Science Foundation of Korea under the grant number NRF-2017R1A2B4003930.

Jinju Kim 7/7/2017 10:00 AM

Deleted: Our calculation shows that sea ice in the sea-ice loss region (21° - 79.5° E \times 75° - 79.5° N) of the Barents and Kara Seas may completely melt by around 2025 (Fig. 1h) unless impeded by other naturally occurring variability. -

Jinju Kim 7/7/2017 10:00 AM

Deleted:

Jinju Kim 7/7/2017 10:00 AM

Deleted: -

References

Árthun, M., Eldevik, T., Smedsrød, L. H., Skagseth, Ø., and Ingvaldsen, R. B.: Quantifying the Influence of Atlantic Heat on Barents Sea Ice Variability and Retreat, *J. Climate*, 25, 4736-4743, 2012.

Bekryaev, R. V., Polyakov, I. V., and Alexeev, V. A.: Role of polar amplification in long-term surface air temperature variation and modern Arctic warming, *J. Climate*, 23, 3888-3906, 2010.

5 Chylek, P., Folland, C. K., Lesins, G., Dubey, M. K., and Wang, M.: Arctic air temperature change amplification and the Atlantic multidecadal oscillation, *Geophys. Res. Lett.*, 36, L14801, doi: 10.1029/2009GL038777, 2009

Cohen, J., Screen, J. A., Furtado, J. C., Barlow, M., Whittleston, D., Coumou, D., Francis J., Dethloff, K., Entekhabi, D., Overland, J., and Jones, J.: Recent Arctic amplification and extreme mid-latitude weather. *Nat. Geosci.*, 7, 627-637, 10 2014.

Comiso, J. C.: Large Decadal Decline of the Arctic Multiyear Ice Cover, *J. Climate* 25, 1176-93, 2012.

Comiso, J. C., Parkinson C. L., Gersten R., and Stock L.: Accelerated decline in the Arctic sea ice cover, *Geophys. Res. Lett.* 35, L01703, doi:10.1029/2007GL031972, 2008.

15 Dee, D., Uppala, S., Simmons, A., Berrisford, P., Poli, P., Kobayashi, S., Andrae, U., Balmaseda, M., Balsamo, G., Bauer, P., Bechtold, P., Beljaars, A. C. M., van de Berg, L., Bidlot, J., Bormann, N., Delsol, C., Dragani, R., Fuentes, M., Geer, A. J., Haimberger, L., Healy, S. B., Hersbach, H., Hólm, E. V., Isaksen, L., Källberg, P., Köhler, M., Matricardi, M., McNally, A. P., Monge-Sanz, B. M., Morcrette, J. J., Park, B. K., Peubey, C., de Rosnay, P., Tavolato, C., Thépaut, J. N., and Vitart, F.: The ERA-Interim reanalysis: Configuration and performance of the data assimilation system, *Q. J. Roy. Meteor. Soc.*, 137, 553-597, 2011

20 Deser, C., Walsh, J. E., and Timlin, M. S.: Arctic sea ice variability in the context of recent atmospheric circulation trends, *J. Climate*, 13, 617-633, 2000.

Deser, C., Tomas, R., Alexander, M., and Lawrence, D.: The Seasonal Atmospheric Response to Projected Arctic Sea Ice Loss in the Late Twenty-First Century, *J. Climate*, 23, 333-351, 2010.

Francis, J. A. and Hunter, E.: Changes in the fabric of the Arctic's greenhouse blanket, *Environ. Res. Lett.*, 2, 045011, 25 doi:10.1088/1748-9326/2/4/045011, 2007.

Graversen, R. G. and Wang, M.: Polar amplification in a coupled climate model with locked albedo, *Clim. Dynam.*, 33, 629-643, 2009.

Graversen, R. G., Mauritsen, T., Tjernström, M., Källén, E., and Svensson, G.: Vertical structure of recent Arctic warming, *Nature*, 451, 53-56, 2008.

30 Holland, M. M. and Bitz, C. M.: Polar amplification of climate change in coupled models, *Clim. Dynam.*, 21, 221-232, 2003.

IPCC, Climate change 2013: The physical science basis. Contribution of Working Group I to the Fifth Assessment Report of the Intergovernmental Panel on Climate Change, edited by: Stocker, T.F., Qin, D., Plattner, G.-K., Tignor, M.,

Allen, S.K., Boschung, J., Nauels, A., Xia, Y., Bex, V., and Midgley, P. M., Cambridge University Press, Cambridge, United Kingdom and New York, NY, USA, 2013.

Kim, B.-M., Son, S.-W., Min, S.-K., Jeong, J.-H., Kim, S.-J., Zhang, X., Shim, T., and Yoon, J.-H.; Weakening of the stratospheric polar vortex by Arctic sea-ice loss, *Nat. Commun.*, 5, doi:10.1038/ncomms5646, 2014.

5 Kim, K.-Y. and North, G. R.: EOFs of harmonizable cyclostationary processes, *J. Atmos. Sci.*, 54, 2416-2427, 1997.

Kim, K.-Y. and Son, S.-W.: Physical characteristics of Eurasian winter temperature variability, *Environ. Res. Lett.*, 11, 044009, 2016.

Kim, K.-Y., North, G. R., and Huang, J.: EOFs of one-dimensional cyclostationary time series: Computations, examples, and stochastic modeling, *J. Atmos. Sci.*, 53, 1007-1017, 1996.

10 Kim, K.-Y., Hamlington, B. D., and Na, H.: Theoretical foundation of cyclostationary EOF analysis for geophysical and climatic variables: Concepts and examples, *Earth-Sci. Rev.*, 150, 201-218, doi:10.1016/j.earscirev.2015.06.003, 2015.

Kim, K.-Y., Hamlington, B. D., Na, H., and Kim, J.; Mechanism of seasonal Arctic sea ice evolution and Arctic amplification, *The Cryosphere*, 10, 2191-2202, doi:10.5194/tc-10-2191-2016, 2016.

15 Koenigk, T., Brodeau, L., Graversen, R. G., Karlsson, J., Svensson, G., Tjernström, M., Willén, U., and Wyser, K.: Arctic climate change in 21st century CMIP5 simulations with EC-Earth, *Clim. Dynam.*, 40, 2719-2743, 2013.

Kumar, A., Perlitz, J., Eischeid, J., Quan, X., Xu, T., Zhang, T., Hoerling, M., Jha, B., and Wang, W.: Contribution of sea ice loss to Arctic amplification, *Geophys. Res. Lett.*, 37, L21701, doi: 10.1029/2010GL045022, 2010.

Mori, M., Watanabe, M., Shiogama, H., Inoue, J., and Kimoto, M.: Robust Arctic sea-ice influence on the frequent Eurasian 20 cold winters in past decades, *Nat. Geosci.*, 7, 869-873, 2014.

Onarheim, I. H., Eldevik, T., Árthun, M., Ingvaldsen, R. B., and Smedsrød, L. H.: Skillful prediction of Barents Sea ice cover, *Geophys. Res. Lett.*, 42, 5364-5371, 2015.

Overland, J. E., Wood, K. R., and Wang, M.: Warm Arctic-cold continents: climate impacts of the newly open Arctic Sea, *Polar Res.*, 30, 15787, 2011.

25 Park, D.-S., Lee, S., and Feldstein, S. B.: Attribution of the recent winter sea ice decline over the Atlantic sector of the Arctic Ocean, *J. Climate*, 28, 4027-4033, 2015a.

Park, H.-S., Lee, S., Son, S.-W., Feldstein, S. B., and Kosaka, Y.: The impact of poleward moisture and sensible heat flux on Arctic winter sea ice variability, *J. Climate*, 28, 5030-5040, 2015b.

Petoukhov, V. and Semenov, V.: A link between reduced Barents-Kara sea ice and cold winter extremes over northern 30 continents, *J. Geophys. Res.*, 115, D21111, doi:10.1029/2009jd013568, 2010.

Schlichtholz, P.: Influence of oceanic heat variability on sea ice anomalies in the Nordic Seas, *Geophys. Res. Lett.*, 38, L05705, doi:10.1029/2010GL045894, 2011.

Schweiger, A. J., Lindsay, R. W., Vavrus, S., and Francis, J. A.: Relationships between Arctic sea ice and clouds during autumn, *J. Climate*, 21, 4799-4810, 2008

Screen, J. A. and Simmonds, I.: The central role of diminishing sea ice in recent Arctic temperature amplification, *Nature*, 464, 1334-1337, doi:10.1038/nature09051, 2010a.

Screen, J. A. and Simmonds, I.: Increasing fall-winter energy loss from the Arctic Ocean and its role in Arctic temperature amplification, *Geophys. Res. Lett.*, 37, L16707, doi:10.1029/2010GL044136, 2010b

5 Screen, J. A., Simmonds, I., Deser, C., and Tomas, R.: The atmospheric response to three decades of observed Arctic sea ice loss, *J. Climate*, 26, 1230-1248, 2013.

Serreze, M. C. and Barry, R. G.: Processes and impacts of Arctic amplification: A research synthesis, *Global Planet Change*, 77, 85-96, 2011.

Serreze, M. C. and Francis, J. A.: The Arctic amplification debate, *Climatic Change*, 76, 241-264, 2006.

10 Serreze, M. C., Holland, M. M., and Stroeve, J.: Perspectives on the Arctic's Shrinking Sea-Ice Cover, *Science*, 315, 1533-1536, 2007.

Serreze, M. C., Barrett, A. P., Stroeve, J. C., Kindig, D. N., and Holland, M. M.: The emergence of surface-based Arctic amplification, *The Cryosphere*, 3, 11-19, 2009.

Smedsrød, L. H., Easu, I., Ingvaldsen, R. B., Eldevik, T., Haugan, P. M., Li, C., Lien, V. S., Olsen, A., Omar, A. M., Otterå, 15 O. H., Risebrobakken, B., Sandø, A. B., Semenov, V. A., and Sorokina, S. V.: The role of the Barents Sea in the Arctic climate system, *Rev. Geophys.*, 15, 415-449, 2013.

Spielhagen, R. F., Werner, K., Sørensen, S. A., Zamelczyk, K., Kandiano, E., Budeus, G., Husum, K., Marchitto, T. M., and Hald, M.: Enhanced Modern Heat Transfer to the Arctic by Warm Atlantic Water, *Science*, 331, 450-453, 2011.

Tang, Q., Zhang, X., Yang, X., and Francis, J. A.: Cold winter extremes in northern continents linked to Arctic sea ice loss, 20 Environ. Res. Lett., 8, 014036, doi:10.1088/1748-9326/8/1/014036, 2013.

Vihma, T.: Effects of Arctic sea ice decline on weather and climate: a review, *Surv. Geophys.*, 35, 1175-1214, 2014.

Figure Captions

Figure 1. Winter (Dec. 1-Feb. 28) average patterns of sea ice loss mode: (a) sea ice (shading) and 2 m air temperature (contour), (b) 1000-850 hPa specific humidity, (c) upward longwave radiation, (d) downward longwave radiation, (e) turbulent (sensible + latent) heat flux, (f) 850 hPa air temperature, (g) the corresponding amplitude change (red solid curve) and the amplification curve (blue dashed curve), and (h) actual sea ice change in the sea-ice loss region (21° - 79.5° E \times 75° - 79.5° N; the boxed area in (a)) of the Barents and Kara Seas (black dotted curve, [extended until 2017 based on new data](#)), sea ice change according to the sea ice loss mode (red curve), projection based on the amplification curve (blue dashed curve). [The red curve in Fig. 1h is obtained by multiplying the loading vector of sea ice concentration \(Fig. 1a\) averaged in the boxed area with the amplitude time series \(Fig. 1g\) according to \(1\).](#) The green contours in (b)-(f) represent sea ice concentration in (a). The numbers in parenthesis are contour intervals and negative contours are dashed.

Figure 2. [Anomalous daily sea ice concentration \(blue\) and upward longwave radiation averaged over the region of sea ice loss \(\$21^{\circ}\$ - \$79.5^{\circ}\$ E \$\times\$ \$75^{\circ}\$ - \$79.5^{\circ}\$ N\) with respective mean values \(straight lines\). Winter days are counted from December 1.](#)

Figure 3. Winter-averaged patterns of [anomalous atmospheric condition: \(a\) 2m air temperature, \(b\) lower tropospheric \(1000-900 hPa\) geopotential height and wind, \(c\) vertical cross section along \$60^{\circ}\$ E of lower tropospheric \(1000-850 hPa\) air temperature, geopotential height and wind, and \(d\) along \$80^{\circ}\$ N. Contour intervals are in parenthesis in \(a\) and \(b\). Temperature is in shading \(0.4 K\), geopotential height is in black contours \(3 m\), and \(c\) zonal and \(d\) meridional winds are in blue contours \(0.2 m s⁻¹\).](#)

Figure 4. Winter-averaged patterns of (a) 850 hPa air temperature (shading) and 2 m air temperature (contour), (b) 900-hPa specific humidity (shade) and downward longwave radiation at surface (contour), (c) net (upward minus downward) longwave radiation at surface (shade) and SAT (contour), and (d) [total cloud liquid water \(shade\) and total cloud ice water \(contour\) for the sea ice loss mode. The red contour is drawn at the value of the contour interval. The green contours in \(a\)-\(d\) represent the reduction of sea ice concentration.](#)

Figure 5. Winter average pattern of sea ice loss mode in the Barents and Kara Seas: (a) sea ice (%), shading), 2 m air temperature (red contour) and 850 hPa temperature (black contour), (b) upward longwave radiation (red contour) and downward longwave radiation (black contour), (c) sensible heat flux (red contour) and latent heat flux (black contour), and (d) net energy balance (sensible heat flux + latent heat flux + upward longwave radiation – downward longwave radiation).

Figure 6. Daily patterns of variability over the region of sea ice loss (21° - 79.5° E \times 75° - 79.5° N): (a) upward longwave radiation (blue dashed), downward longwave radiation (blue dotted), net longwave radiation (blue solid) with its mean value (blue straight line), sensible heat flux (red dashed), latent heat flux (red dotted), and turbulent heat flux (red solid) with its mean value (red straight line), (b) 2 m air temperature (red), 850 hPa air temperature \times 2 (black), and upward longwave radiation (blue), and (c) same as (b) except for the regressed downward longwave radiation (blue). The straight lines in (b) and (c) represent the winter mean value of anomalous 2 m air temperature. Correlation of upward and downward longwave radiations with 2 m air temperature is respectively 0.88 and 0.91, whereas with 850 hPa air temperature is 0.66 and 0.85.

Jinju Kim 7/7/2017 10:25 AM

Deleted: and purple

Jinju Kim 7/7/2017 10:01 AM

Deleted: (a) Anomalous daily sea ice concentration and (b) upward longwave radiation averaged over the region of sea ice loss (21° - 79.5° E \times 75° - 79.5° N). Winter days are counted from December 1.

Jinju Kim 7/7/2017 10:02 AM

Deleted: 925 hPa air temperature,

Jinju Kim 7/7/2017 10:02 AM

Deleted: total cloud cover for the sea ice loss mode.

Jinju Kim 7/7/2017 10:24 AM

Deleted: and purple

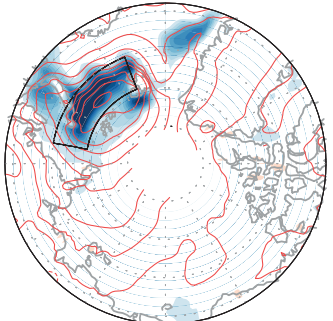
Figure 7. Lagged correlations: (a) correlation of upward (solid lines) and downward (dotted lines) longwave radiations with 2 m air temperature (blue), 850 hPa temperature (red), and sea ice concentration (black), and (b) a blow-up of the boxed region in (a). Longwave radiation lags the other variable for a positive lag. Lagged correlation between 2 m air temperature and 850 hPa air temperature (black dashed line); 2 m air temperature leads 850 hPa temperature for a positive lag.

5 **Figure 8.** A proposed mechanism of polar amplification. Increased net upward energy flux increases air temperature. As a result, downward longwave radiation increases, which results in ~~sea ice melting~~. This loop seems to amplify by ~8.9% annually.

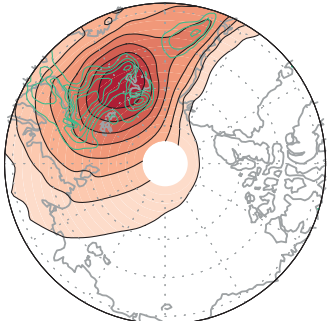
Jinju Kim 7/7/2017 10:03 AM

Deleted: warmer surface temperature and

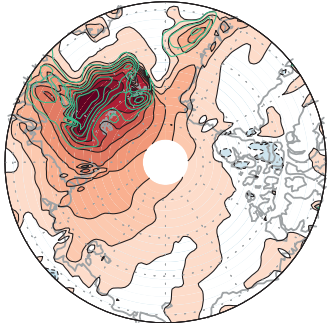
(a) SIC (2 %) & 2m AIRT (0.5° C)



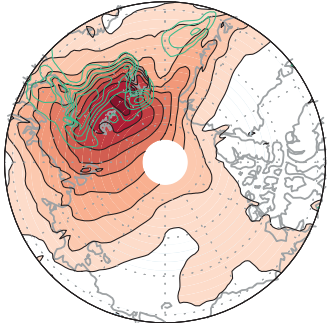
(b) 1000-850 hPa SH ($3 \times 10^{-2} \text{ g Kg}^{-1}$)



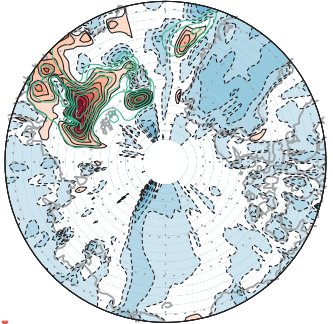
(c) ULW at SFC (2 W m^{-2})



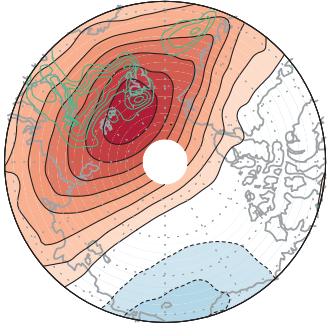
(d) DLW at SFC (2 W m^{-2})



(e) TURBULENT FLUX (4 W m^{-2})

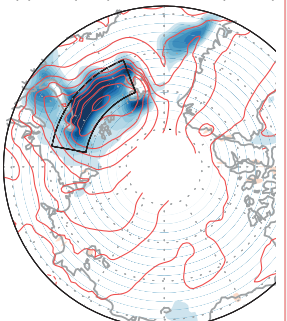


(f) 850 hPa T (0.2° C)

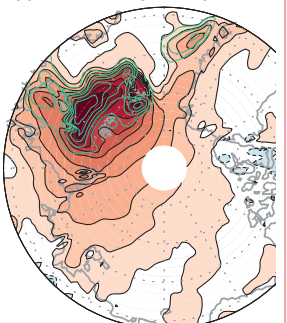


Jinju Kim 7/7/2017 10:07 AM

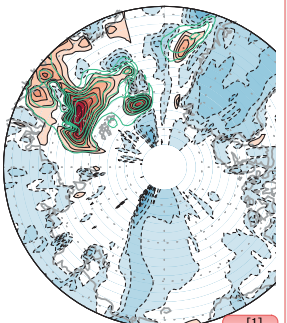
(a) SIC (2 %) & 2m AIRT (0.5° C)



(c) ULW at SFC (2 W m^{-2})



(e) TURBULENT FLUX (4 W m^{-2})



Deleted:

... [1]

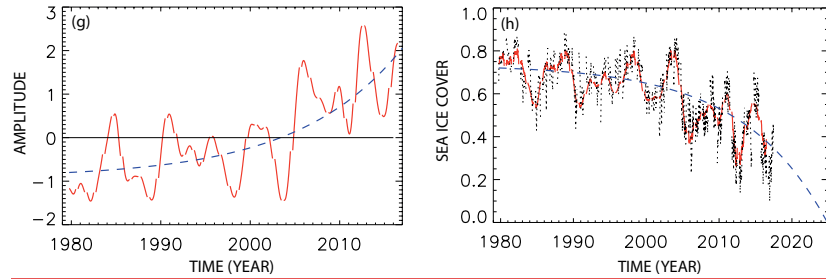


Figure 1. Winter (Dec. 1-Feb. 28) average patterns of sea ice loss mode: (a) sea ice (shading) and 2 m air temperature (contour), (b) 1000-850 hPa specific humidity, (c) upward longwave radiation, (d) downward longwave radiation, (e) turbulent (sensible + latent) heat flux, (f) 850 hPa air temperature, (g) the corresponding amplitude change (red solid curve) and the amplification curve (blue dashed curve), and (h) actual sea ice change in the sea-ice loss region (21° – 79.5° E \times 75° – 79.5° N; the boxed area in (a) of the Barents and Kara Seas (black dotted curve, extended until 2017 based on new data), sea ice change according to the sea ice loss mode (red curve), projection based on the amplification curve (blue dashed curve). The red curve in Fig. 1h is obtained by multiplying the loading vector of sea ice concentration (Fig. 1a) averaged in the boxed area with the amplitude time series (Fig. 1g) according to (1). The green contours in (b)–(f) represent sea ice concentration in (a). The numbers in parenthesis are contour intervals and negative contours are dashed.

Jinju Kim 7/7/2017 10:25 AM
Deleted: and purple

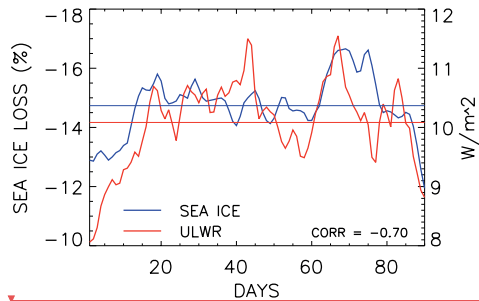
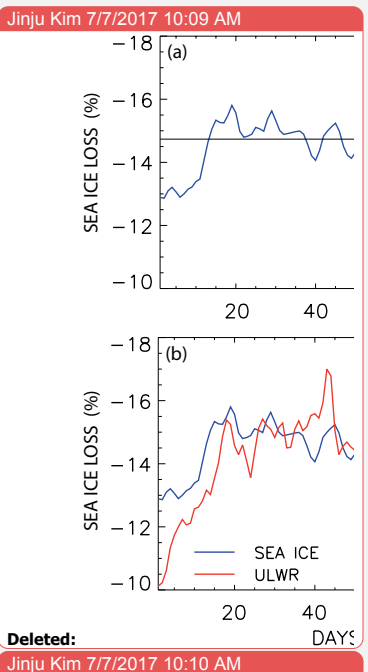


Figure 2. Anomalous daily sea ice concentration (blue) and upward longwave radiation averaged over the region of sea ice loss (21° - 79.5° E \times 75° - 79.5° N) with respective mean values (straight lines). Winter days are counted from December 1.



Deleted:

Jinju Kim 7/7/2017 10:10 AM

Deleted: (a) Anomalous daily sea ice concentration and (b) upward longwave radiation averaged over the region of sea ice loss (21° - 79.5° E \times 75° - 79.5° N). Winter days are counted from December 1.

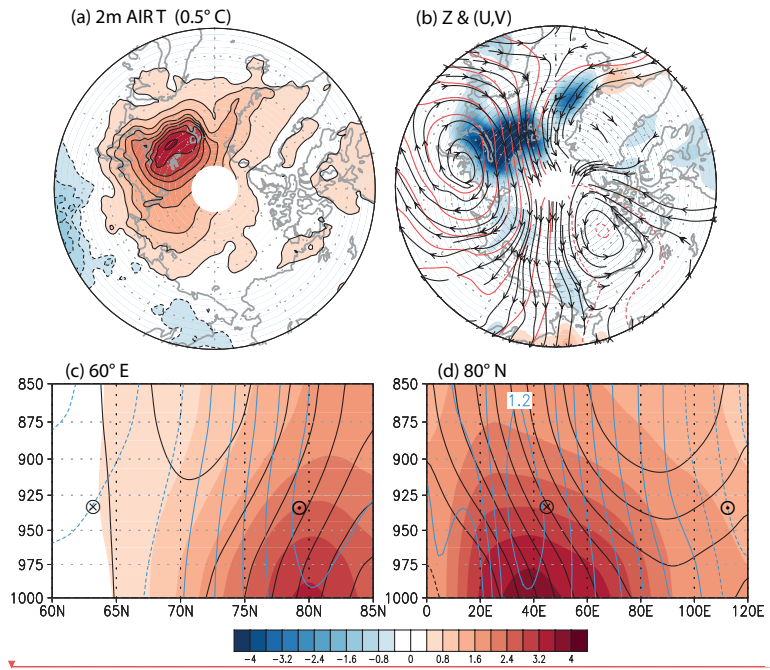
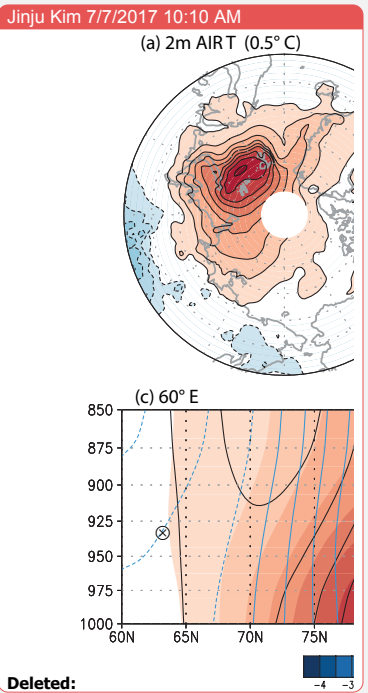


Figure 3. Winter-averaged patterns of anomalous atmospheric condition: (a) 2 m air temperature, (b) lower tropospheric (1000-900 hPa) geopotential height and wind, (c) vertical cross section along 60° E of lower tropospheric (1000-850 hPa) air temperature, geopotential height and wind, and (d) along 80° N. Contour intervals are in parenthesis in (a) and (b). Temperature is in shading (0.4 K), geopotential height is in black contours (3 m), and (c) zonal and (d) meridional winds are in blue contours (0.2 m s^{-1}).



Jinju Kim 7/7/2017 10:11 AM

Deleted: 925 hPa air temperature

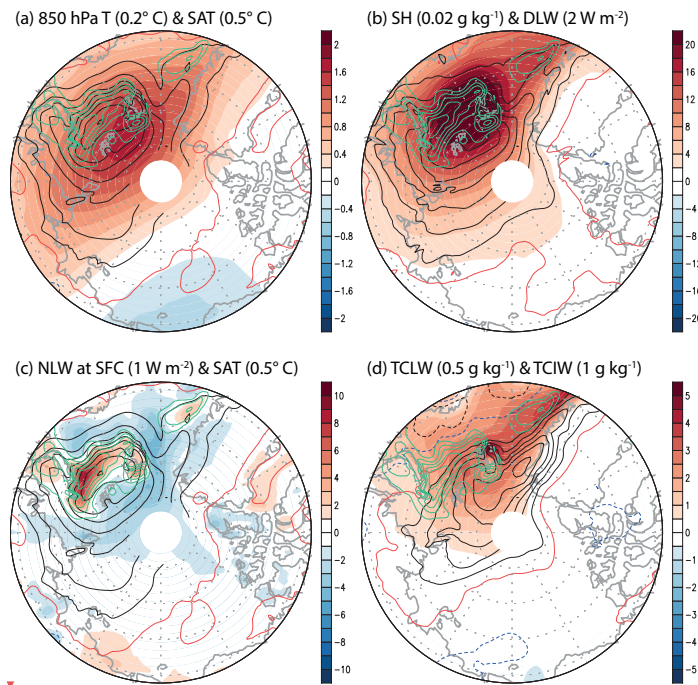
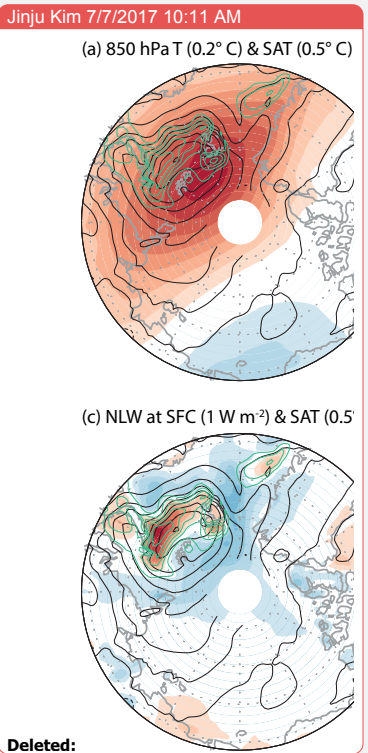


Figure 4. Winter-averaged patterns of (a) 850 hPa air temperature (shading) and 2 m air temperature (contour), (b) 900-hPa specific humidity (shading) and downward longwave radiation at surface (contour), (c) net (upward minus downward) longwave radiation at surface (shading) and SAT (contour), and (d) total cloud liquid water (shading) and total cloud ice water (contour) for the sea ice loss mode. The red contour is drawn at the value of the contour interval. The green contours in (a)-(d) represent the reduction of sea ice concentration.



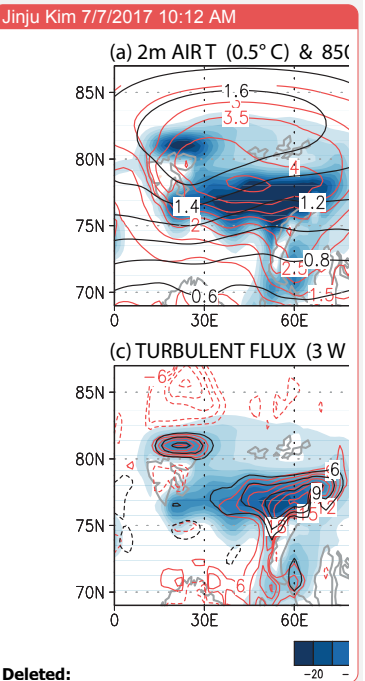
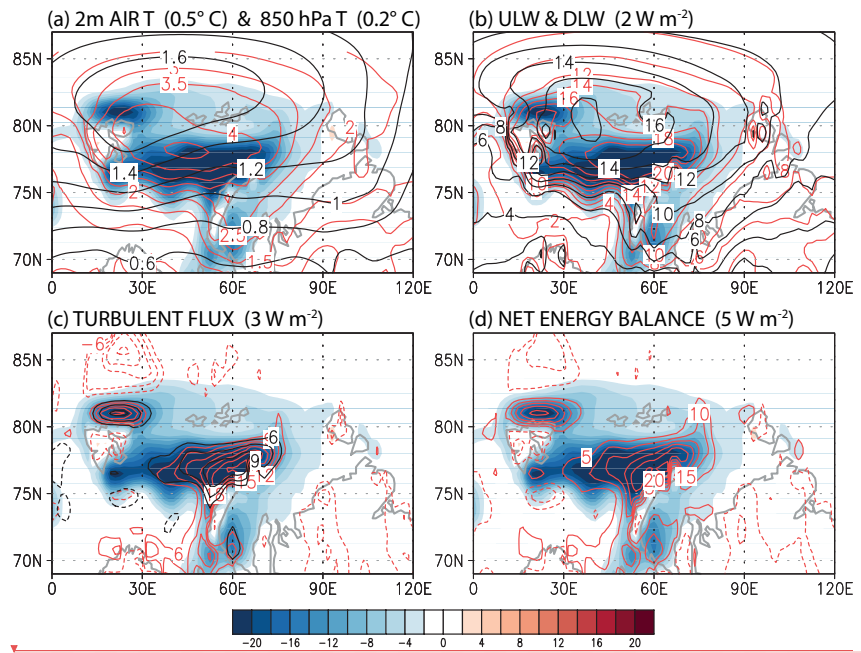


Figure 5. Winter average pattern of sea ice loss mode in the Barents and Kara Seas: (a) sea ice (%), shading), 2 m air temperature (red contour) and 850 hPa temperature (black contour), (b) upward longwave radiation (red contour) and downward longwave radiation (black contour), (c) sensible heat flux (red contour) and latent heat flux (black contour), and (d) net energy balance (sensible heat flux + latent heat flux + upward longwave radiation – downward longwave radiation).

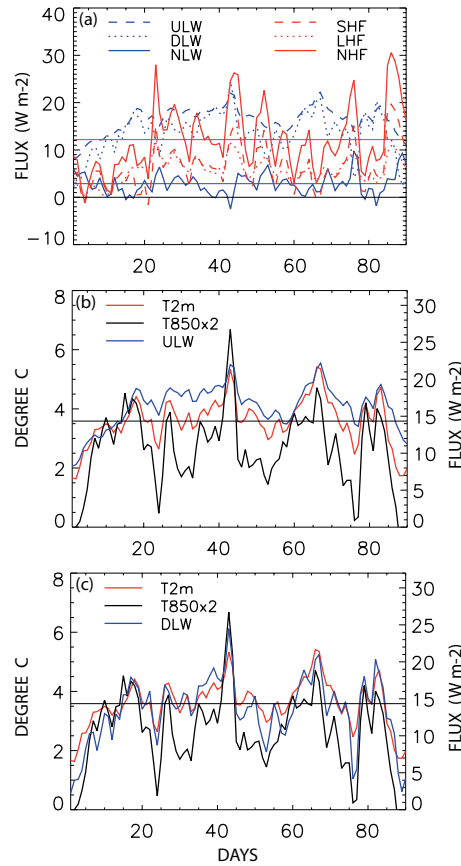


Figure 6. Daily patterns of variability over the region of sea ice loss (21°-79.5° E × 75°-79.5° N): (a) upward longwave radiation (blue dashed), downward longwave radiation (blue dotted), net longwave radiation (blue solid) with its mean value (blue straight line), sensible heat flux (red dashed), latent heat flux (red dotted), and turbulent heat flux (red solid) with its mean value (red straight line), (b) 2 m air temperature (red), 850 hPa air temperature × 2 (black), and upward longwave radiation (blue), and (c) same as (b) except for the regressed downward longwave radiation (blue). The straight lines in (b) and (c) represent the winter mean value of anomalous 2 m air temperature. Correlation of upward and downward longwave radiations with 2 m air temperature is respectively 0.88 and 0.91, whereas with 850 hPa air temperature is 0.66 and 0.85.

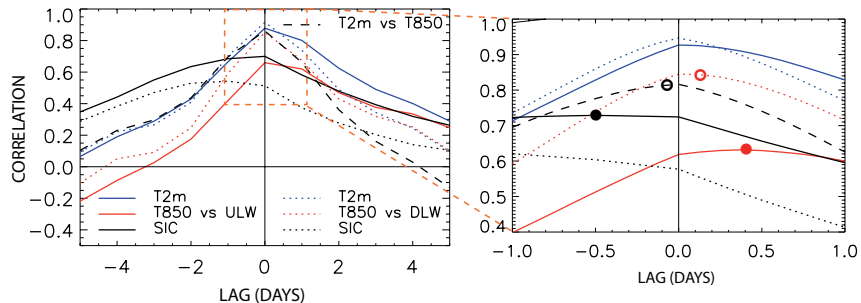
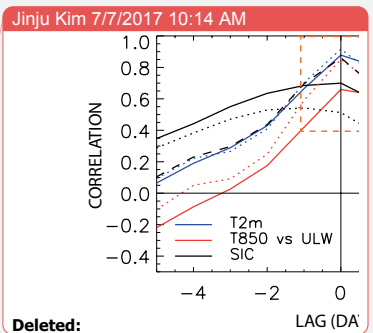


Figure 7. Lagged correlations: (a) correlation of upward (solid lines) and downward (dotted lines) longwave radiations with 2 m air temperature (blue), 850 hPa temperature (red), and sea ice concentration (black), and (b) a blowup of the boxed region in (a). Longwave radiation lags the other variable for a positive lag. Lagged correlation between 2 m air temperature and 850 hPa air temperature (black dashed line); 2 m air temperature leads 850 hPa temperature for a positive lag.



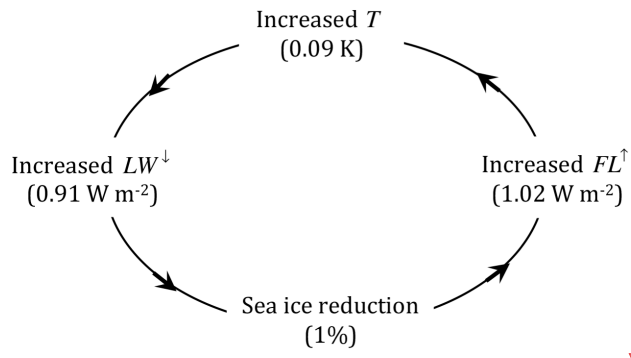


Figure 8. A proposed mechanism of polar amplification. Increased net upward energy flux increases air temperature. As a result, downward longwave radiation increases, which results ~~and~~ sea ice melting. This loop seems to amplify by ~8.9 % annually.

Jinju Kim 7/7/2017 10:15 AM

Formatted: Centered

Jinju Kim 7/7/2017 10:15 AM

Deleted: <sp>

Jinju Kim 7/7/2017 10:15 AM

Deleted: in warmer surface temperature

Supplementary Information

Understanding the Mechanism of Arctic Amplification and Sea Ice Loss

5 Kwang-Yul Kim¹, Jinju Kim¹, Saerim Yeo², Hanna Na³, Benjamin D. Hamlington⁴, and Robert R. Leben⁵

¹School of Earth and Environmental Sciences, Seoul National University, 1 Gwanak-ro, Gwanak-gu, Seoul 08826, Republic of Korea

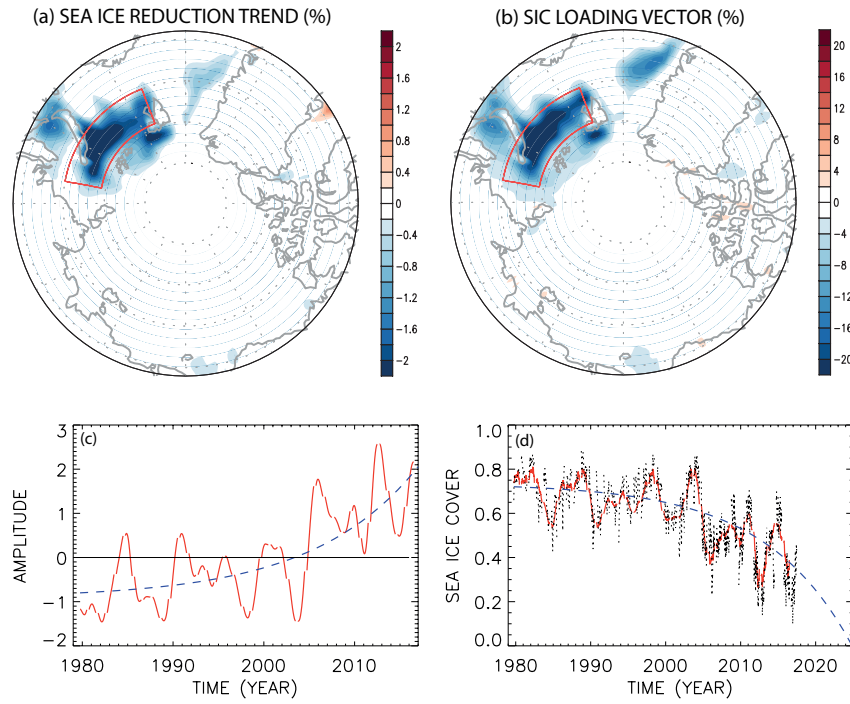
²APEC Climate Center 1463, Haeundae-gu, Busan 48058, Republic of Korea

10 ³Ocean Circulation and Climate Research Center, Korea Institute of Ocean Science and Technology, Ansan, 15627, Republic of Korea

⁴Department of Ocean, Earth and Atmospheric Sciences, 4600 Elkhorn Avenue, Room 406, Old Dominion University, Norfolk, Virginia 23529, USA

⁵Colorado Center for Astrodynamics Research, Department of Aerospace Engineering Sciences, ECNT 320, 431 UCB, University of Colorado, Boulder, Colorado 80309-0431, USA

15 *Correspondence to:* Kwang-Yul Kim (kwang56@snu.ac.kr)



5 **Figure S1.** (a) The yearly trend (%) of sea ice reduction in the Arctic Ocean during 1979-2016, (b) the winter averaged loading vector of the sea ice loss mode, (c) the corresponding PC (amplitude) time series, and (d) actual sea ice concentration in the boxed area (black curve), sea ice concentration according to the sea ice loss mode (red curve) and a projection (red dashed curve) based on the exponential fit of the amplitude time series in (c).

10

Figure S1a is obtained based on a linear trend of sea ice concentration at each grid point based on the ERA-Interim sea ice concentration from 1979-2016. This pattern is nearly identical with the sea ice loss mode discussed in the main text (Fig. S1b). Sea ice reduction is most conspicuous in the Barents-Kara Seas. The amount of sea ice reduction based on the sea ice loss mode is obtained by multiplying the loading vector (Fig. S1b) with its amplitude time series (Fig. S1c), resulting in Fig. 15 S1d. As can be seen in Fig. S1d, the sea ice concentration change due to the sea ice loss mode (red curve) is similar to the actual data (black curve) with a fairly similar rate of trend.

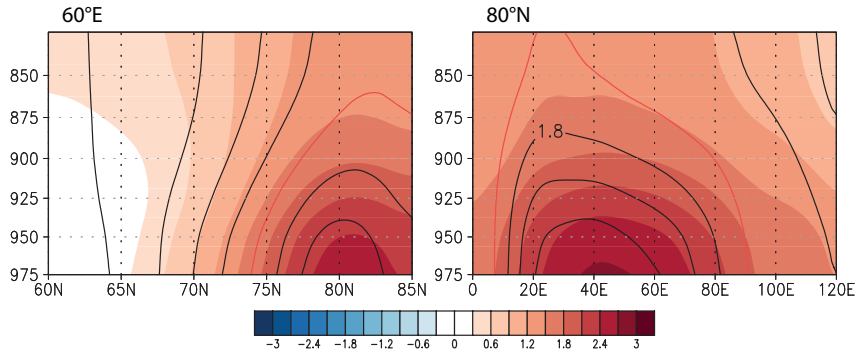


Figure S2. The pressure layer thickness ($\Delta Z = Z(p_1) - Z(p_0)$) derived from the geopotential height pattern in Fig. 3 in the text and that derived from the hydrostatic equation (contour). The red contour represents the thickness of 1.5 m. The level 5 p_1 is the level used for plotting and p_0 is the pressure level below p_1 at the interval of 25 hPa.

The shaded geopotential height anomaly in this figure is obtained directly from the geopotential height field in Fig. 3 in the main text, i.e.,

$$10 \quad (dZ)_j = Z_j - Z_{j-1}, \quad (1)$$

where j is an index for the vertical level. The contoured geopotential height anomaly is obtained from the temperature field in Fig. 3 in the text, i.e.,

$$(dZ)_j = -\frac{R\langle T \rangle_j}{g} (d \ln p)_j, \quad (2)$$

where

$$15 \quad (dZ)_j = Z_j - Z_{j-1}, \quad \langle T \rangle_j = (T_j + T_{j-1})/2, \quad (d \ln p)_j = \ln p_j - \ln p_{j-1}. \quad (3)$$

As can be seen in the figure, the anomalous geopotential height field is nearly in hydrostatic balance with the anomalous temperature field. The difference is partially due to the use of layer mean temperature $\langle T \rangle$ in a finite-difference approximation of the hydrostatic equation in (2). Thus, it seems that the release of energy in the form of radiation and heat flux changes the temperature, and geopotential height in the lower troposphere adjusts in accordance with the hydrostatic balance.

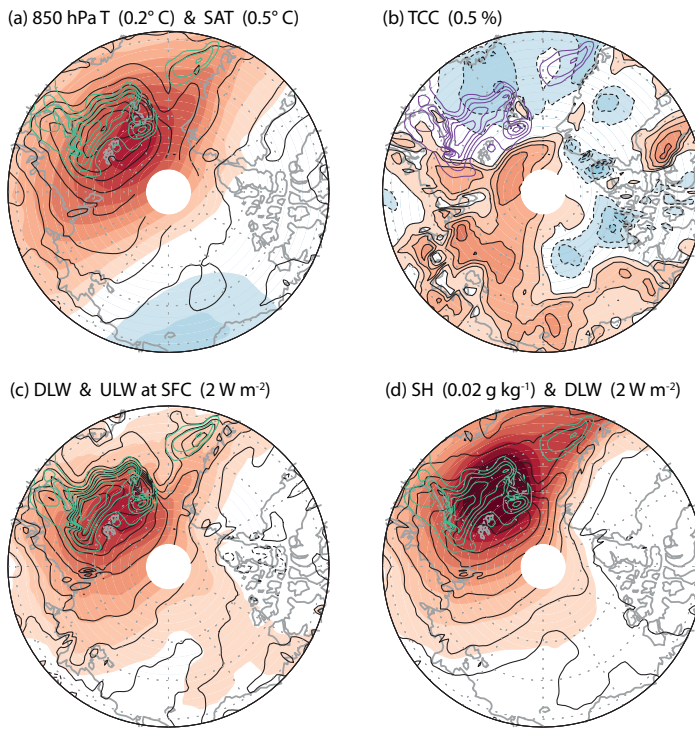


Figure S3. The DJF patterns of 850 hPa air temperature (shading) and 2 m air temperature (contour) (a), total cloud cover (b), downward (shade) and upward (contour) longwave radiation at surface (c), and 900-hPa specific humidity (shading) and downward longwave radiation at surface (contour) (d) for the sea ice loss mode. The green and purple contours in (a)-(d) represent the reduction of sea ice concentration.

This figure shows the winter (DJF) averaged patterns of several key variables associated with the sea ice reduction. As can
 10 be seen, anomalous patterns of all the variables exhibit strong coherence with that of sea ice reduction except for total cloud cover. The pattern of total cloud cover associated with the sea ice loss mode does not exhibit any strong cloud activity over the region of sea ice reduction, suggesting little connectivity between sea ice reduction and change in cloud cover. However, total cloud liquid water and total cloud ice water, which are two important elements for the production of clouds are reasonably consistent with the pattern of sea ice reduction (see Fig. 4 in the main text).

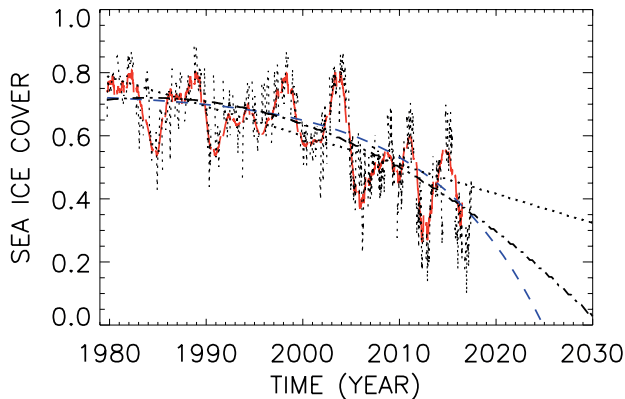


Figure S4. Actual sea ice change in the sea-ice loss region (21° – 79.5° E, 75° – 79.5° N) of the Barents and Kara Seas (black dotted curve; updated until Feb. 2017 using new dataset), sea ice change according to the sea ice loss mode (red curve),
 5 projections based on the exponential fitting (blue dashed curve), quadratic fitting (dash-dot curve), and linear fitting (dotted curve) of the PC time series.

This figure shows projections of sea ice concentration in the sea-ice loss region of the Barent-Kara Seas based on a linear fit
 10 (dotted curve), a quadratic fit (dash-dot curve), and an exponential fit (dashed). Residual variance is measured by

$$\varepsilon^2 = \text{var}(S(t) - F(t)),$$

where $S(t)$ is the sea ice concentration curve (black curve in Fig. S4) and $F(t)$ is a fit. The exponential fit results in the least residual variance, whereas the linear fit the largest residual variance. The residual variance of the quadratic fit is similar to that of the exponential fit. Sea ice in the region (21° – 79.5° E, 75° – 79.5° N) disappears completely by 2025 (2030, 2065)
 15 according to the exponential (quadratic, linear) fit. According to the newly available data, sea ice concentration in this area is the lowest during 2016 winter (Dec. 2016-Feb. 2017; see the dotted line in Fig. S4).

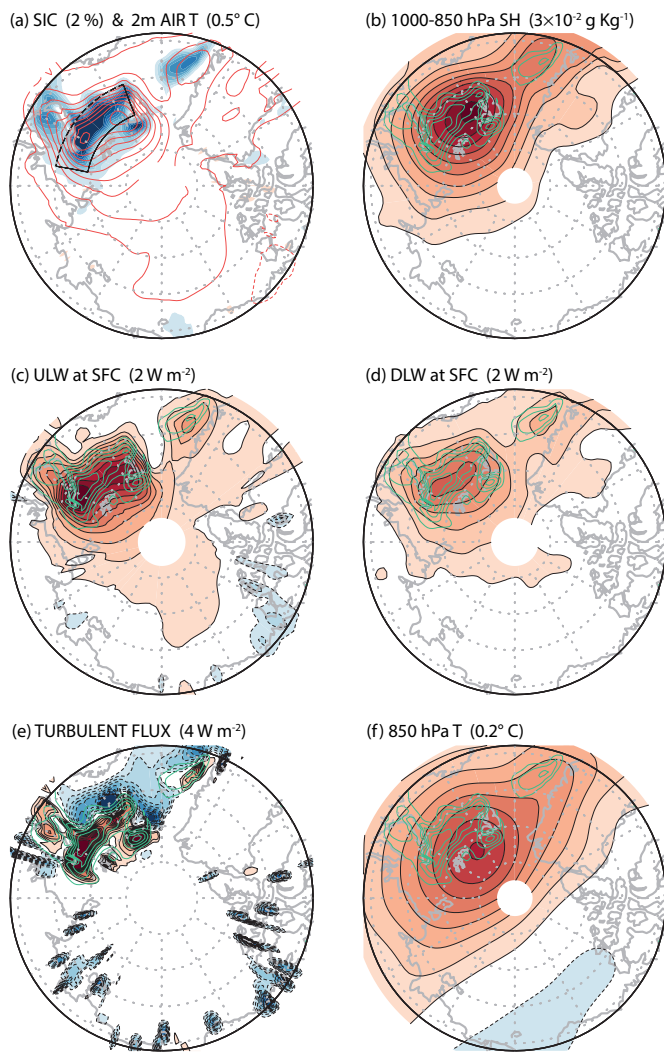


Figure S5. Winter (Dec. 1-Feb. 28) average patterns of sea ice loss mode derived from the NCEP reanalysis data: (a) sea ice (shading) and 2 m air temperature (contour), (b) 1000-850 hPa specific humidity, (c) upward longwave radiation, (d) downward longwave radiation, (e) turbulent (sensible + latent) heat flux, (f) 850 hPa air temperature.

5

This figure shows the winter-averaged patterns of key variables from the NCEP reanalysis product (1979-2016) associated with the sea ice loss mode. The target variable is the ERA-Interim sea ice concentration as in the main text. This figure is fairly similar to Fig. 1a-f in the text except for a small difference in magnitude. Thus, an essentially identical physical process is identified in the NCEP reanalysis product. This result indicates that the physical mechanism addressed in the present study is not overly sensitive to the choice of the dataset for analysis.

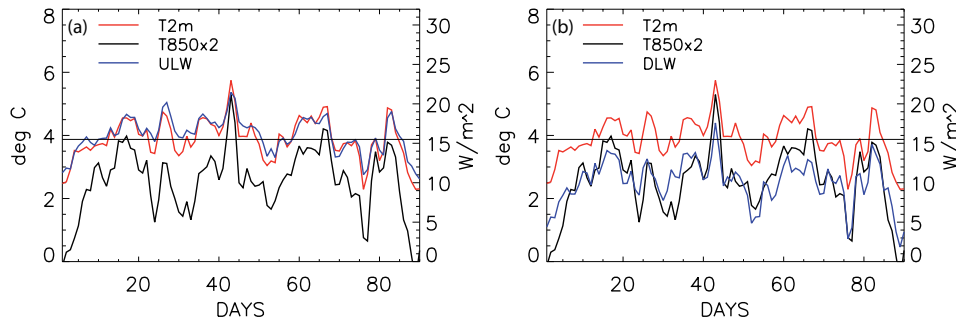


Figure S6. Daily pattern of variability over the region of sea ice loss (21° - 79.5° E \times 75° - 79.5° N) derived from the NCEP reanalysis data: (a) 2 m air temperature (red), 850 hPa air temperature $\times 2$ (black), and upward longwave radiation (blue), and (b) same as (a) except for the regressed downward longwave radiation (blue). The straight line represents the winter 5 mean value of anomalous 2 m air temperature. Correlation of upward and downward longwave radiation with 2 m air temperature is respectively 0.95 and 0.94, whereas correlation with 850 hPa air temperature is respectively 0.81 and 0.86.

This figure shows the daily evolution of surface (2 m) air temperature, 850 hPa air temperature, upward longwave radiation 10 and downward longwave radiation during winter in response to sea ice reduction in the Barents-Kara Seas as in Fig. 2 in the main text. This result is obtained by using the NCEP reanalysis data. A comparison with Fig. 6 in the main text shows that the response of atmospheric variables to the sea ice reduction in the Barents-Kara Seas as identified from the NCEP reanalysis product is fairly similar to that derived from the ERA-Interim reanalysis product. This figure together with Fig. S4 indicates that the physical process of sea ice reduction and Arctic warming discussed in the text is not sensitive to the 15 choice of analysis dataset.